

The characteristics of EMIC waves observed by the Van Allen Probes and Arase satellites

Chae-Woo Jun¹, Yoshizumi Miyoshi¹, Satoshi Kurita², Chao Yue³, Jacob Bortnik⁴, Larry Lyons⁵, S Nakamura¹, Masafumi Shoji¹, Shun Imajo¹, Craig Kletzing⁶, Yoshiya Kasahara⁷, Yasumasa Kasaba⁸, Shoya Matsuda⁹, Fuminori Tsuchiya⁸, Atsushi Kumamoto¹⁰, Ayako Matsuoka¹¹, and Iku Shinohara¹²

¹Nagoya University

²Kyoto Daigaku

³Peking University

⁴University of California, Los Angeles

⁵AOS/UCLA, Los Angeles, USA

⁶University of Iowa, Iowa, USA

⁷Kanazawa University

⁸Tohoku University

⁹ISAS/JAXA, Tokyo, Japan

¹⁰Tohoku University, Tohoku University

¹¹Kyoto University

¹²Japan Aerospace Exploration Agency

November 22, 2022

Abstract

We performed a comprehensive statistical study of electromagnetic ion cyclotron (EMIC) waves observed by the Van Allen Probes and Exploration of energization and Radiation in Geospace satellite (ERG/Arase). From 2017 to 2018, we identified and categorized EMIC wave events with respect to wavebands (H⁺ and He⁺ EMIC waves) and relative locations from the plasmasphere (inside and outside the plasmasphere). We found that H-band EMIC waves in the morning sector at L>8 are predominantly observed with a mixture of linear and right-handed polarity and higher wave normal angles during quiet geomagnetic conditions. Both H⁺ and He⁺ EMIC waves observed in the noon sector at L[~]4-6 have left-handed polarity and lower wave normal angles at |MLAT|< 20° during the recovery phase of a storm with moderate solar wind pressure. In the afternoon sector (12-18 MLT), He-band EMIC waves are dominantly observed with strongly enhanced wave power at L[~]6-8 during the storm main phase, while in the dusk sector (17-21 MLT) they have lower wave normal angles with linear polarity at L>8 during geomagnetic quiet conditions. Based on distinct characteristics at different EMIC wave occurrence regions, we suggest that EMIC waves in the magnetosphere can be generated by different free energy sources. Possible sources include the freshly injected particles from the plasma sheet, adiabatic heating by dayside magnetospheric compressions, suprathermal proton heating by magnetosonic waves, and off-equatorial sources.

Hosted file

essoar.10505039.1.docx available at <https://authorea.com/users/537417/articles/600050-the-characteristics-of-emic-waves-observed-by-the-van-allen-probes-and-arase-satellites>

The characteristics of EMIC waves observed by the Van Allen Probes and Arase satellites

C.-W Jun^{1*}, Y. Miyoshi¹, S. Kurita², S. Nakamura¹, M. Shoji¹, S. Imajo¹, C. Yue³, J. Bortnik⁴, L. Lyons⁴, C. Kletzing⁵, Y. Kasahara⁶, Y. Kasaba⁷, S. Matsuda⁸, F. Tsuchiya⁶, A. Kumamoto⁶, A. Matsuoka⁸, and I. Shinohara⁸

¹ Institute for Space-Earth Environmental Research (ISEE), Nagoya University, Nagoya, Japan

² Kyoto University, Kyoto, Japan

³ Peking University, Beijing, China

⁴ AOS/UCLA, Los Angeles, USA

⁵ University of Iowa, Iowa, USA

⁶ Kanazawa University, Kanazawa, Japan

⁷ Tohoku University, Sendai, Japan

⁸ ISAS/JAXA, Tokyo, Japan

Corresponding author: Chae-Woo Jun (chae-woo@isee.nagoya-u.ac.jp)

Key Points:

- EMIC waves in the magnetosphere have four major occurrence regions excited by possibly different generation processes.
- For He-EMIC waves in the afternoon sector, injected particles and off-equatorial source are the major driver at $L \sim 6$ and $L > 8$, respectively.
- H-EMIC waves are generated by enhancing dynamic pressure in the noon sector at $L < 6$, or suprathermal protons in the dawn sector at $L > 8$.

Abstract

We performed a comprehensive statistical study of electromagnetic ion cyclotron (EMIC) waves observed by the Van Allen Probes and Exploration of energization and Radiation in Geospace satellite (ERG/Arase). From 2017 to 2018, we identified and categorized EMIC wave events with respect to wavebands (H^+ and He^+ EMIC waves) and relative locations from the plasmasphere (inside and outside the plasmasphere). We found that H-band EMIC waves in the morning sector at $L > 8$ are predominantly observed with a mixture of linear and right-handed polarity and higher wave normal angles during quiet geomagnetic conditions. Both H^+ and He^+ EMIC waves observed in the noon sector at $L \sim 4-6$ have left-handed polarity and lower wave normal angles at $|\text{MLAT}| < 20^\circ$ during the recovery phase of a storm with moderate solar wind pressure. In the afternoon sector (12-18 MLT), He-band EMIC waves are dominantly observed with strongly enhanced wave power at $L \sim 6-8$ during the storm main phase, while in the dusk sector (17-21 MLT) they have lower wave normal angles with linear polarity at $L > 8$ during geomagnetic quiet conditions. Based on distinct characteristics at different EMIC wave occurrence regions, we suggest that EMIC waves in the magnetosphere can be generated by different free energy sources. Possible sources include the freshly injected particles from the plasma sheet, adiabatic heating by dayside magnetospheric compressions, suprathermal proton heating by magnetosonic waves, and off-equatorial sources. (225 words)

1 Introduction

Electromagnetic ion cyclotron (EMIC) waves have been considered to play a fundamental role in controlling the dynamics of the radiation belts and ring current particles by wave-particle interactions (e.g., Anderson et al., 1992a, 1992b; Kuwashima et al., 1981; Thorne, 2010). Particularly, wave-particle interactions involving EMIC waves constitute a significant loss process of energetic protons and sub-relativistic electrons through pitch-angle scattering, contributing to the creation of the isolated proton aurora observed at subauroral latitudes (e.g., Miyoshi et al., 2008; Sakaguchi et al., 2007, 2008; Usanova et al., 2010) and drive the loss of relativistic electrons in the radiation belt below 2 MeV energies (e.g., Miyoshi et al., 2008; Jordanova et al., 2008; Hyun et al., 2014; Usanova et al., 2010).

EMIC waves are typically observed in the frequency range of 0.1-5 Hz. They are detected between ion gyrofrequencies and can be categorized as three wavebands: H⁺ EMIC waves between the proton gyrofrequency and helium gyrofrequency, He⁺ EMIC waves between the helium gyrofrequency and oxygen gyrofrequency, and O⁺ EMIC waves below the oxygen gyrofrequency (e.g., Chen et al., 2010).

Numerous studies have reported spatial distributions of EMIC waves in the magnetosphere using data from satellite observations: Active Magnetospheric Particle Tracer Explorer/Charge Composition Explorer (AMPTE/CCE; e.g., Anderson et al., 1992a, 1992b; Keika et al., 2013), Time History of Events and Macroscale Interactions during Substorms (THEMIS; e.g., Min et al., 2012; Usanova et al., 2012; Kim et al., 2016; Nakamura et al., 2014), Cluster (Allen et al., 2015, 2016), Geostationary Operational Environmental Satellite (e.g., Park et al., 2016), Combined Release and Radiation Effects Satellite (CRRES; e.g., Halford et al., 2010; Meredith et al., 2014), Van Allen Probes (RBSP; e.g., Saikin et al., 2015; Wang et al., 2015; Jun et al., 2019a, 2019b; Yue et al., 2019), Magnetospheric Multiscale mission (e.g., Wang et al., 2017; Vines et al., 2019), and Exploration of energization and Radiation in Geospace (ERG/Arase; e.g., Matsuda et al., 2018a). These previous studies found that EMIC waves can be detected over a wide range of magnetic local times (MLT) of 3-21 MLT and L values from 3-15. These waves are also observed at higher magnetic latitude (MLAT) due to propagation from the wave sources near the magnetic equator. Using data from THEMIS observation, Usanova et al. (2012) found EMIC waves have a higher occurrence rate on the dayside magnetosphere than the nightside, and these waves are frequently observed beyond geosynchronous orbit at high L-shells with the occurrence rate over 10%. Min et al. (2012) found that He⁺ EMIC waves have a peak occurrence at dusk and 8-12 R_E, while H EMIC waves are common at dawn and 10-12 R_E. Using RBSP observations, Jun et al. (2019a) found He⁺ EMIC waves are predominantly observed inside the plasmasphere while the majority of EMIC waves outside the plasmasphere are in the H band.

Temperature anisotropy ($T_{\parallel} < T_{\perp}$) of energetic ions, where T_{\parallel} and T_{\perp} are the parallel and perpendicular components of temperatures with respect to the ambient magnetic field, plays the important role in ions cyclotron instability, leading to the generation of EMIC waves in the magnetosphere (Cornwall et al., 1970; Horne and Thorne, 1994). Direct evidence of the generation of EMIC waves through wave-particle interactions was obtained by the WPIA analysis that identifies relative phase differences between gyrating ions and waves (Shoji et al.,

2017). Using data from the RBSP satellites, Yue et al (2019) found that EMIC waves have the highest wave occurrence near the magnetic equator with left-handed polarization and relatively small wave normal angles, suggesting that these waves are locally generated near the threshold of proton anisotropy instability.

Freshly injected energetic ions in the energy range of 1-100 keV are transported from the plasma sheet due to large-scale magnetospheric convection during active geomagnetic conditions (e.g., Axford, 1969; Yue et al., 2017a, 2017b). As these particles interact with cold, dense plasmaspheric plasma in the afternoon sector at $L=4-7$, the temperature anisotropy causes the generation of EMIC waves (e.g., Saikin et al., 2016; Jun et al., 2019a; Yue et al., 2019, 2020). Using RBSP observation, Teng et al. (2019) performed a statistical study of unusual high-frequency EMIC waves with simultaneously observed magnetosonic waves. The author proposed that magnetosonic waves cause the resonant heating, leading to the pancake distribution of suprathermal protons (10-100 eV). Such suprathermal protons can contribute to the growth of EMIC waves near the proton gyrofrequency with a narrow bandwidth. They found these waves were mainly observed from the dawn to the dusk sector in the low-density regions. Using data from AMPTE/CCE satellite, Keika et al. (2013) found that He^+ EMIC waves are observed more frequently during the main phase of the storm than the recovery phase in the afternoon side in the outer magnetosphere ($L>7$). In the inner magnetosphere, Saikin et al. (2016) found that increasing AE index leads to the peak occurrence region of EMIC waves shifting from noon to the afternoon sector at $L\sim 4-6$. Using data from RBSP and GOES satellites, Jun et al. (2019b) reported that EMIC waves associated with particle injections are predominantly observed in the afternoon sector with the most intense wave power in the He band.

Dayside magnetospheric compression by enhanced solar wind dynamic pressure leads to an increase in temperature anisotropy of energetic ions due to adiabatic heating on the dayside (e.g., Anderson and Hamilton, 1993; McCollough et al., 2010; Yue et al., 2009, 2010, 2011). Previous studies have been considered that this is one of the major drivers of EMIC waves on the dayside magnetosphere (e.g., Arnoldy et al., 2005; Engebretson et al., 2002; Nakamura et al., 2014; Olson and Lee, 1983; Park et al., 2016; Remya et al., 2017; Tsurutani et al., 2016; Usanova et al., 2008, 2012; Jun et al., 2019b). Based on RBSP observations, Jun et al. (2019b) performed a statistical study and found the H^+ EMIC waves observed outside the plasmasphere were accompanied by a solar wind dynamic pressure enhancement on the dayside regardless of injections. Using GOES observations, Park et al. (2016) suggested that solar wind pressure is the major parameter for the generation of EMIC waves during quiet geomagnetic conditions ($K_p \leq 1$) at geosynchronous orbit.

Previous studies have suggested that EMIC waves can also be generated at off-equatorial source regions located at higher latitudes in the dayside outer magnetosphere due to magnetospheric compression (e.g., Allen et al., 2015, 2016; Vines et al., 2019). Drift-shell splitting and executing Shabansky orbits is the mechanism that is believed to cause an increase in the temperature anisotropy of energetic ions that become trapped in the off-equatorial source regions at higher-L shells (McCollough et al., 2012).

In addition, plasmaspheric EMIC waves are known to be generated through several different mechanisms. It was recently shown that mode conversion from the magnetosonic mode waves in addition to cyclotron resonance could be in operation, and mode conversion from

lightning whistlers (Miyoshi et al., 2019). They showed that generation of oblique EMIC waves from the magnetosonic mode waves due to enhancement of M/Q=2 ions in lower L-shells from RBSP and Arase. Horne and Miyoshi (2016) theoretically predicted that parallel EMIC waves can be generated from mode conversion of magnetosonic mode waves when the wave normal angle of the magnetosonic mode waves becomes parallel.

In our previous studies (Jun et al., 2019a and 2019b), we focused on the relationship between EMIC wave generation and injected energetic particles in the inner magnetosphere ($L < 6.5$) using the RBSP observations. In this study, we perform a comprehensive study of spatial distributions of EMIC wave properties and their dependence on geomagnetic activity. We emphasize that this paper is the first to use both RBSP and Arase observations to identify numerous EMIC wave events, which allows us to extend the observable L and MLAT coverage to $L=3-12$ and $|\text{MLAT}| < 50^\circ$, respectively. We have also found four different peak wave occurrence regions of EMIC waves, which have unique wave properties under different geomagnetic environments. Thus, we believe our statistical results provide new insight for improving our understanding of EMIC wave dynamics in the magnetosphere.

In Section 2, we describe the instruments used in this statistical study, and the methods used for data analysis. In Section 3, we present the statistical results. In Section 4 we propose possible generation mechanisms of EMIC waves in the magnetosphere, and we summary our results and suggest future works in Section 5.

2 Observations

2.1 Instrumentation

The Van Allen Probes (RBSP), two identical spacecraft (A and B), were launched on August 30, 2012. They have an identical elliptical orbit with perigee and apogee of 1.1 RE to 5.8 RE, and a period of ~ 9 h with an inclination of 10° , (Mauk et al., 2013). This study utilizes the Electric and Magnetic Field Instrument Suite and Integrated Science (EMFISIS) magnetometer that measures the direct current (DC) magnetic field (Kletzing et al., 2013).

The Arase satellite was launched on December 20, 2016, and the available data starts from March 2017 (Miyoshi et al., 2018a). The perigee and apogee of this satellite are 400 km and 6 RE, respectively. A period is ~ 9.5 h with the orbital inclination of Arase is 31° . In this study, we used instruments including: The Magnetic Field Experiment, measuring the low-rate (64/256 Hz) magnetic field waveform (MGF; Matsuoka et al., 2018); The Plasma Wave Experiment (PWE) (Kasahara et al., 2018). The PWE consists of the following receivers: The Electric Field Detector (EFD; Kasaba et al., 2017); the Waveform Capture/Onboard Frequency Analyzer (WFC/OFA; Matsuda et al., 2018b); and the High-Frequency Analyzer (HFA; Kumamoto et al., 2018).

We utilized SYM-H, time-shifted (to the Earth's bow shock nose) solar wind dynamic pressure (P_{dyn}), and AL index to determine the relationship between EMIC wave activity and the geomagnetic condition from the OMNI database (<https://omniweb.gsfc.nasa.gov>) with a time resolution of 1 min.

2.2 Data Analysis

In this study, we rotated the magnetic field data obtained from the EMFISIS and MGF instrument onboard the RBSP and Arase into a mean-field-aligned (MFA) coordinate system (Takahashi et al., 1990). The mean-field is calculated with a moving average time window of 32 s. By definition of MFA coordinate system, the x-, y-, and z-components are the radial, azimuthal, and parallel directions of the ambient magnetic field, respectively. We then applied a fast Fourier transform to the data set to obtain the spectral matrix of each component for further wave analysis. We set a time window of 64 s (4,096 data points) and 15 s moving window, so the frequency and time resolutions are 0.0156 Hz and 15 s, respectively.

Using the obtained spectral matrix, we adopt a wave analysis method as described in Section 2.2 of Jun et al. 2019b, in order to obtain the various wave parameters (power density spectrum, wave normal angle, polarization sense, polarization ratio, and coherence) in the frequency domain. The wave normal angle (θ) is the angle between the wave propagation direction and the ambient magnetic field, that is between 0 - 90° . The polarization sense (ϵ) is the ratio of the minor axis to the major axis. The sign of ϵ is the rotation direction of the magnetic field, implying that positive and negative ϵ corresponds to right-hand (RH) and left-hand (LH) polarities, respectively. We computed the polarization ratio and coherence, in order to clarify the reliable wave properties from the background noise. The polarization ratio is the ratio of

polarized power to total power and the coherence represents the relationship between two signals. If two signals are nearly identical and propagated from the same source, the coherence is close to 1, while a coherence of zero indicates no relationship between them.

2.3 Data collection

EMIC waves were identified for a 24-month period from January 2017 to December 2018. In this period, the RBSP and Arase data set are sufficient to fully cover all MLT regions as shown in Figure 2. We adopt the EMIC wave event selection criteria as described in Jun et al. 2019a. First, the center frequency of EMIC waves must be observed below the equatorial proton gyrofrequency derived from the estimated equatorial field intensity. Second, we took their wave powers over 10^{-4} nT²/Hz and a minimum duration longer than 5 min in the dynamic spectra by visual inspection. We also set the coherence and polarization ratio threshold of 0.5 to identify appropriate EMIC waves from background noise. Then, we excluded some events having strong parallel components such as magnetosonic waves. In the case of harmonic-like events detected with multi-band structures simultaneously, we took the fundamental wave as an individual case. The waveband for each event was defined by the equatorial ion gyrofrequencies, instead of the local magnetic field intensity. In this study, we only took into account H⁺ and He⁺ EMIC waves due to lower oxygen gyrofrequency below 0.1 Hz at the apogee location of the satellites. It is difficult to distinguish the event from overlapping broadband emissions (e.g., PiB bursts and Pc 3-5 pulsations) or other background noise.

In addition, the L values and the equatorial field intensity are calculated by using 2004 Tsyganenko and Sitnov magnetic field model (TS04; Tsyganenko and Sitnov, 2005). The relative location of the satellites from the plasmapause (inside and outside the plasmasphere) for each event was determined using background electron density profile derived by upper hybrid resonance frequency as described in Jun et al. (2019a). We identified the plasmapause crossing when electron density varied at least a factor of 5 within a distance of 0.5 in L (Moldwin et al., 2002; Kurth et al., 2015).

As shown in Figure 1, an EMIC wave event is observed on 30 January 2018 at 0820-1105 UT detected by the Arase. Figures 1a-1c show geomagnetic indices: SYM-H (Figure 1a), averaged AL index (Figure 1b), and averaged solar wind dynamic pressure P_{dyn} (Figure 1c). Figures 1d-1i show the observations from the Arase: an electron density profile derived from the upper hybrid frequency (Figure 1d), the perpendicular component of the magnetic field in the dynamic spectrum (Figure 1e), polarization ratio (Figure 1f), coherence (Figure 1g), polarization sense ε (Figure 1h), and wave normal angle θ (Figure 1i) in the frequencies of 0.3-0.8 Hz. Arase was located around 11 MLT and MLAT=3° at L~6 in the noon sector for this event. During this time interval, SYM-H, averaged AL and P_{dyn} varied around -15 nT, -400 nT, and 5 nPa, respectively, indicating a non-storm time substorm interval (Figures 1a-1c). In Figure 1d, the electron density profile presented no significant variations with a constant value of 200 cm⁻³, indicating that the Arase was inside the plasmasphere. We were able to identify a clear He⁺ EMIC wave event from 0920 to 1005 UT in Figure 1e as marked with two red vertical dashed lines. During the event interval, the polarization ratio and coherence were 0.78 and 0.75,

respectively, in Figures 1f-1g, indicating a typical EMIC wave event. The average ϵ and θ were -0.54 (LH) and 15.47° as shown in Figures 1h-1i.

In order to determine the characteristics of EMIC waves in the inner magnetosphere, we collected the frequency-averaged wave properties (e.g., Jun et al., 2019b). For this process, we first found the frequency boundary, as marked with two red curved dashed lines in Figure 1e, using the following criteria during the wave event interval: wave power $> 10^{-4}$ nT²/Hz, polarization ratio, and coherence > 0.6 . We also selected the center frequency which has the highest wave power within the selected frequency boundary as marked by a blue dashed line in Figure 1e. In this study, we recorded the EMIC wave properties (polarization ratio, coherence, wave power, center frequency, ϵ , and θ) every 1 min during the wave duration, as well as information of the satellite location (MLT, L, and |MLAT|).

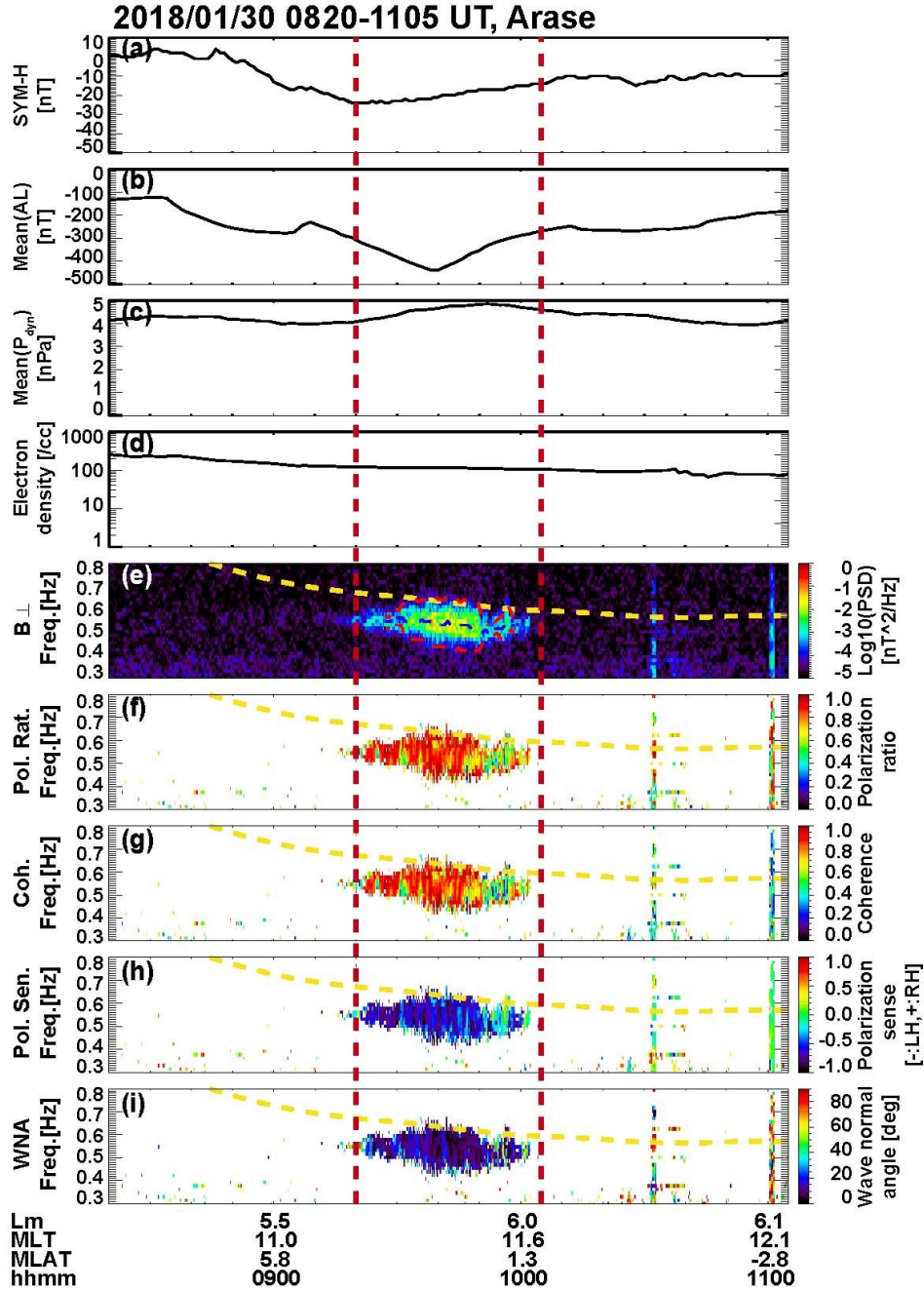


Figure 1. Example of EMIC event observed on 30 January, 2018 at 0820-1105 UT observed by the Arase satellite. (a) SYM-H index, (b) average AL index, (c) average solar wind dynamic pressure (P_{dyn}), Arase observation of (d) electron density, (e) the perpendicular component of the magnetic field (B_{\perp}) dynamic power spectrum obtained by MGF instrument, (f) polarization ratio, (g) coherence, (h) polarization sense ϵ , (i) wave normal angle θ . The red vertical lines indicate the start and end time of the EMIC wave. The red and blue curves in Figure 1e represent the upper and lower frequency boundaries and center frequency of the EMIC wave, respectively. The yellow dashed line denotes the equatorial He^+ gyrofrequency.

3. Statistical results

Based on our event selection criteria, we identified 324.2, 321.7, and 290.2 hrs of EMIC waves observed by the RBSP-A, RBSP-B and Arase, respectively, from January 2017 to December 2018. In this section, we present spatial distributions of EMIC waves, their dependence on geomagnetic conditions, and their wave properties.

3.1 Spatial Distribution of EMIC waves

Figure 2 presents the distributions of total combined dwell times in hours and EMIC wave occurrence rate observed by both the RBSP and Arase satellites in the L-MLT plane (Figures 2a and 2c) and the MLT-MLAT plane (Figures 2b and 2d). By using the projected L values into the magnetic equator, we can extend the L shell coverage to $L=12$. For the L-MLT plane, the bin sizes are 1 h in MLT and 0.5 in L shell. The L shell coverage ranges $L=2$ to 12. We used the bin sizes 1 h in MLT and 5° in MLAT for the MLT-MLAT plane with the MLAT range of -50 - 50° . As we can see in Figures 2a-2b, the combination of the RBSP and Arase satellites provides sufficient observation times over all MLT, L shell, and MLAT. EMIC occurrence rates in each bin are computed as the total EMIC wave observation time divided by the dwell time in that bin as shown in Figures 2c and 2d with a logarithmic color bar range of 1-100 %. The gray regions in Figure 2c denote EMIC wave occurrence rate lower than 1 %.

Overall, EMIC waves are generally observed on the dayside with higher occurrence rate at $L > 6$ compare to the regions at $L < 6$. In particular, we can see clear three major occurrence regions of EMIC waves in the magnetosphere in Figures 2c-2d: 4-8 MLT, $MLAT < -30^\circ$ at $L > 8$ (morning sector), 10-14 MLT, $|MLAT| < 20^\circ$ at $L = 3-6$ (noon sector), and 12-21 MLT, $MLAT > 20^\circ$ at $L = 6-12$ (afternoon sector). Our spatial distribution of EMIC waves is consistent with previous satellite observations (e.g., Halford et al., 2016; Paulson et al., 2016; Saikin et al., 2015; Usanova et al., 2016; Wang et al., 2015; Jun et al., 2019a; Min et al., 2013; Keika et al., 2013).

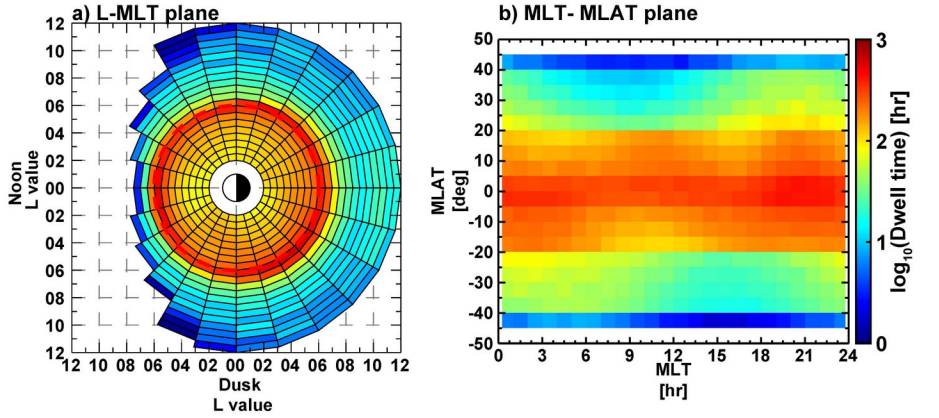
We divided all selected EMIC events into the four groups based on the waveband and relative location from the plasmapause as shown in Figure 3. The format is the same as the overall occurrence rate shown in Figure 2c. The observation times of EMIC waves are 70.2, 276.7, 527.1, and 52.8 hrs for H^+ EMIC waves inside the plasmasphere, H^+ EMIC waves outside the plasmasphere, He^+ EMIC waves inside the plasmasphere, and He^+ EMIC waves outside the plasmasphere, respectively.

Since H^+ EMIC waves inside the plasmasphere have lower wave occurrences less than 1 % at all MLT, any significant peak occurrences are not found in this group (Figure 3a). H^+ EMIC waves are not common phenomena inside the plasmasphere (e.g., Jun et al., 2019a; Yue et al., 2019) and may not provide statistically significant results, we exclude this group from further analyses and discussions.

The spatial distributions of H^+ EMIC waves outside the plasmasphere show two separated peak occurrence regions at 4-8 MLT and 10-14 MLT in Figure 3b. The major peak occurrence region in the morning sector at $L > 8$ is consistent with EMIC wave distributions in the outer

magnetosphere observed by THEMIS satellites (e.g., Min et al., 2013; Kim et al., 2016). The other peak region appears in the noon sector at $L < 6$ near the geosynchronous orbit.

Dwell time of the Van Allen Probes and Arase



EMIC wave occurrence rate of the Van Allen Probes and Arase

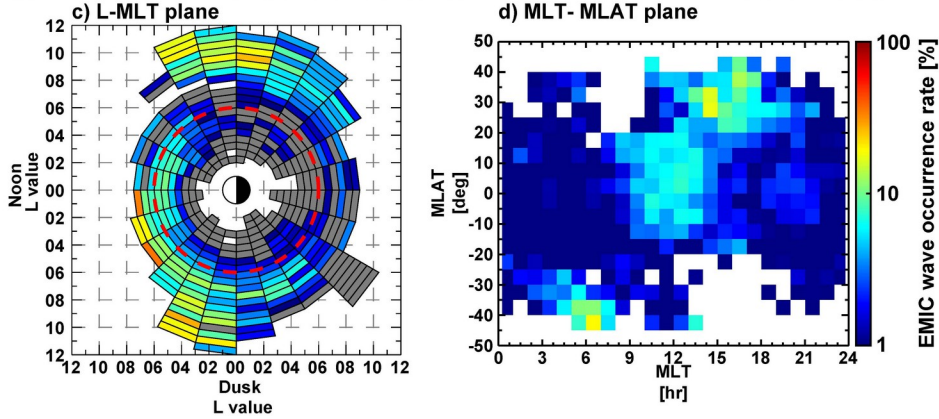


Figure 2. The dwell time in the (a) L-MLT plane and (b) MLT-MLAT plane and EMIC occurrence rate of all EMIC waves in the (c) L-MLT plane and (d) MLT-MLAT plane observed by the RBSP and Arase from January 2017 to December 2018. The gray regions indicate EMIC wave occurrence rate lower than 1 %.

In Figure 3c, He^+ EMIC waves inside the plasmasphere are predominantly observed with a wide spatial coverage at 9-17 MLT and at $L \sim 5-8$, consistent with typical He^+ EMIC wave distributions near the plasmasphere. He^+ EMIC waves are frequently observed in the noon sector at geosynchronous orbit during steady quiet geomagnetic conditions (e.g., Kim et al., 2016; Park et al., 2016; Jun et al., 2019a). The peak occurrence regions of He^+ EMIC waves in the afternoon sector coincides with previous studies of EMIC wave distributions during active geomagnetic conditions (e.g., Saikin et al., 2016; Keika et al., 2013; Usanova et al., 2012; Wang et al., 2015; Jun et al., 2019a).

He^+ EMIC waves outside the plasmasphere are predominantly observed at 16-18 MLT at $L > 8$ in the dusk sector with a clear dawn-dusk asymmetry of the wave occurrence. This

tendency is consistent with previous studies (e.g., Anderson et al., 1992a; Keika et al., 2013; Min et al., 2012) showing that the occurrence rate of He EMIC waves was high at higher L shells in the dusk sector.

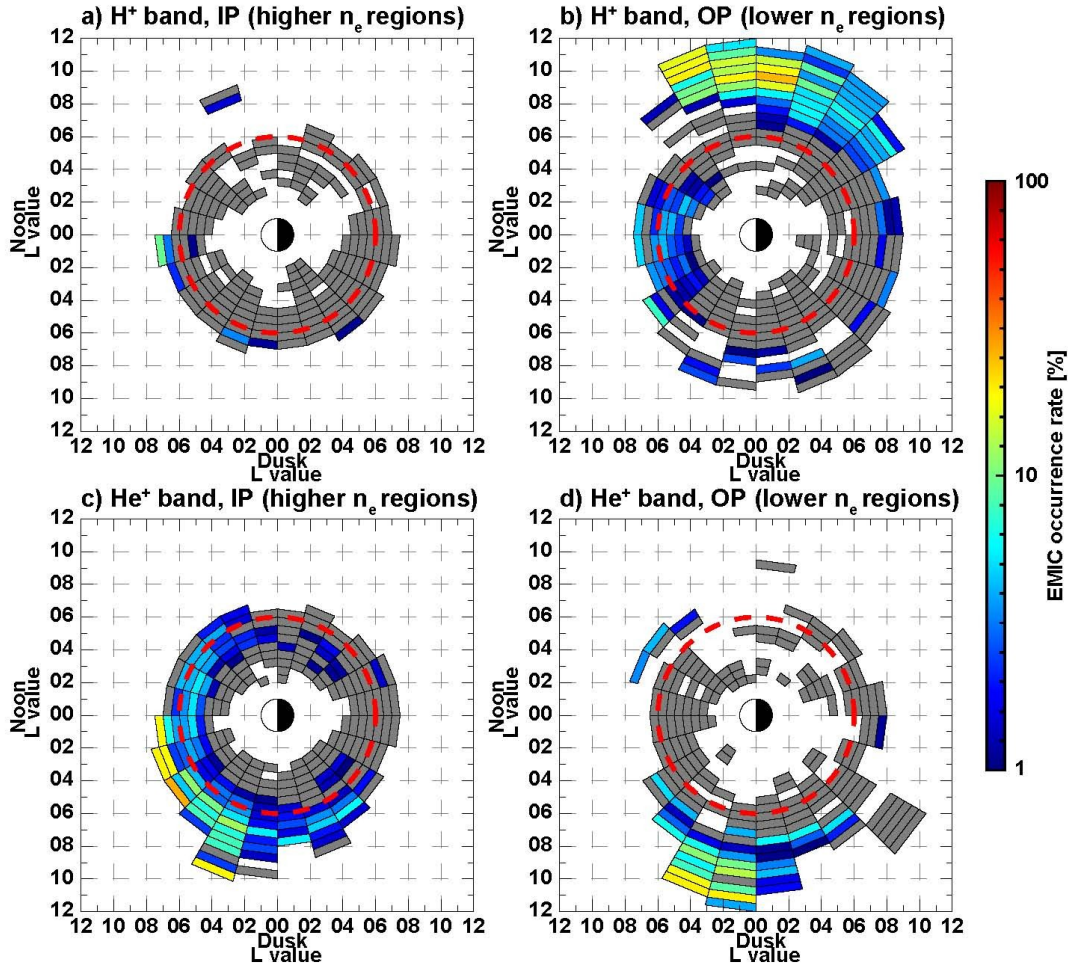


Figure 3. The EMIC occurrence rates for (a) H⁺ band, inside the plasmasphere (IP), (b) H⁺ band, outside the plasmasphere (OP), (C) He⁺ band, IP, and (d) He⁺ band, OP.

3.2 Dependence of EMIC waves on geomagnetic conditions

In this section, we examined EMIC wave events against the SYM-H, AL, and solar wind dynamic pressure (P_{dyn}) in order to demonstrate the relationship between EMIC waves and geomagnetic conditions. SYM-H represents the development of the geomagnetic storm. AL index is used to identify the substorm activity. P_{dyn} corresponds to the magnetospheric compression. We utilized the 1 min OMNI resolution data set. Since the spontaneous values of AL and P_{dyn} are not sufficient as indicators of geomagnetic activities due to different locations to collect data, we averaged AL and P_{dyn} with a time range of T_0 - $T_{0-30 \text{ min}}$, where T_0 represents an arbitrary time point during the wave interval set.

Figure 4 presents the spatial distributions of EMIC waves during different storm phases. We illustrate the identification of a storm phase as shown in Figure 4a. We adopt the identification of the storm phases in the same manner as Halford et al. (2010) and Saikin et al. (2016). We utilized 1 min SYM-H index in order to identify a more accurate storm phase (i.e., no storm interval, prestorm, main, and recovery phase). We selected the geomagnetic storm that the minimum SYM-H must reach a threshold of -40 nT. The main phase of the storm was defined as an interval from the starting point of decreasing SYM-H to the minimum SYM-H. The Δ SYM-H value is defined as the total SYM-H variation during the main phase. The recovery phase is determined from the end of the main phase to the timing when the SYM-H had recovered to 70 % of the Δ SYM-H value. According to Halford et al. (2010), the pre-onset phase was defined as 3 h before the onset of the main phase. However, we did not use this phase due to the limited EMIC wave observation time for the statistics. No-storm interval is defined as the time intervals which is not included in other storm phases. According to our definition, we found total 39 geomagnetic storms in 2017-2018.

During the no-storm interval (Figures 4b-d), EMIC waves are frequently observed at $L > 7$ in all three groups. The higher L shell observations of EMIC waves might be related to the influence of the expanding plasmasphere during quiet geomagnetic conditions (Kwon et al., 2015). Interestingly, we can see a significant peak wave occurrence region in the morning sector at $L > 8$ for H^+ band outside the plasmasphere (Figure 4b), consistent with the previous result reported in Kim et al. (2016) showing that H^+ EMIC wave events observed under quiet geomagnetic conditions ($K_p \leq 1$) mostly contribute to the maximum occurrence rate seen in the early morning sector (06-09 MLT) at the outermost region ($L > 10$) based on the using THEMIS observations.

Figures 4e-4g present the spatial distributions of EMIC wave occurrence rate during the main phase of the storm for each group. Figures 4h-4j are for the recovery phase. During the main phase, only He^+ EMIC waves inside the plasmasphere have a significant wave distribution in the afternoon (10-21 MLT) sector at $L=4-7$ (Figure 4f), while EMIC waves are mainly observed on the dayside of the magnetosphere at $L=4-8$ in the H^+ and He^+ band during the recovery phase (Figures 4h and 4i), except for a peak occurrences in the dusk (17-19 MLT) at $L > 9$ for He^+ EMIC waves outside the plasmasphere. Our EMIC wave occurrence distributions in the main and recovery phases coincide with the storm dependence of EMIC waves done by Keika et al. (2013).

Figures 5 and 6 show spatial distributions of AL and P_{dyn} , respectively. We averaged AL and P_{dyn} values during the wave interval within bins of 1 h in MLT and 0.5 in L. To avoid unreliable results due to low wave occurrences, we only consider the regions in which EMIC wave occurrence rate is ≥ 1 % in a bin.

Figure 5 presents that each peak occurrence region of EMIC waves has a significant dependence on different substorm conditions. In Figure 5a, H^+ EMIC waves in the morning sector are frequently observed under the average AL value of -100 nT, indicating no or very weak substorm interval. On the other hand, the average AL value in the noon sector is approximately -200 nT, meaning that these EMIC waves occurred during the moderate substorm intervals. For He^+ band (Figures 5b and 5c), EMIC waves are mainly detected in the average AL

range of -200 to -400 nT, indicating that strong substorms contribute to the generation of He⁺ EMIC waves in the afternoon sector (e.g., Saikin 2016, Jun et al., 2019a).

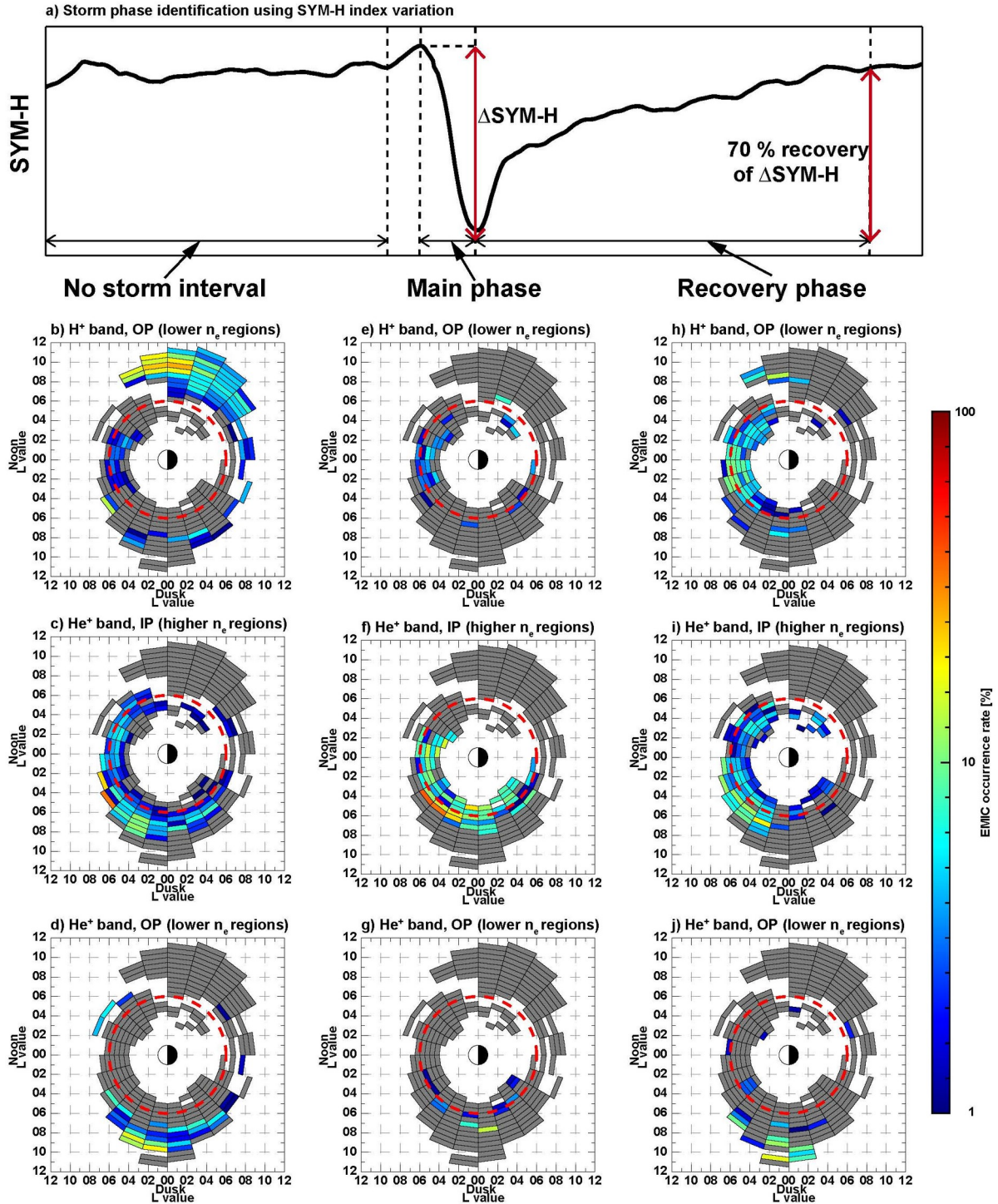


Figure 4. (a) schematic figure of the identification of the storm phase using SYM-H variations. The EMIC occurrence rates during (a-c) no storm interval, (e-g) the main phase of the storm, and (h-j) the recovery phase of the storm.

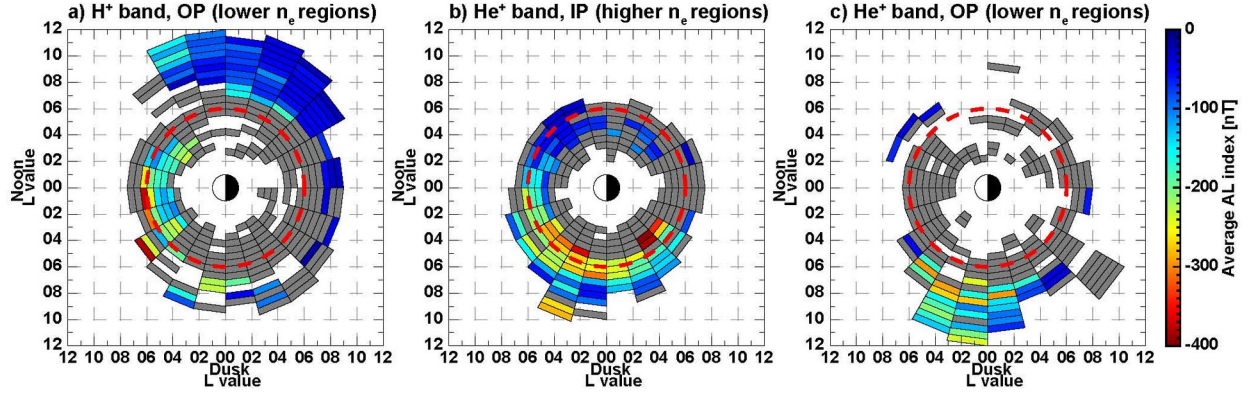


Figure 5. The spatial distribution of average AL index for (a) H⁺ band, OP, (b) He⁺ band, IP, and (C) He⁺ band, OP.

Figure 6 shows the spatial distribution of average P_{dyn} during the wave events. The major distributions of EMIC waves with a P_{dyn} value over 3 nPa are in the noon and afternoon sector for the H⁺ and He⁺ band, respectively (Figures 6a and 6b). This observational result is consistent with previous studies (e.g., Usanova et al., 2012; Park et al., 2016) showing an increase in EMIC wave occurrence due to magnetospheric compression on the dayside of the magnetosphere. On the other hand, EMIC waves in the morning and dusk sector for H⁺ and He⁺ band are frequently observed below 3 nPa, indicating that these waves may be not related to magnetospheric compressions.

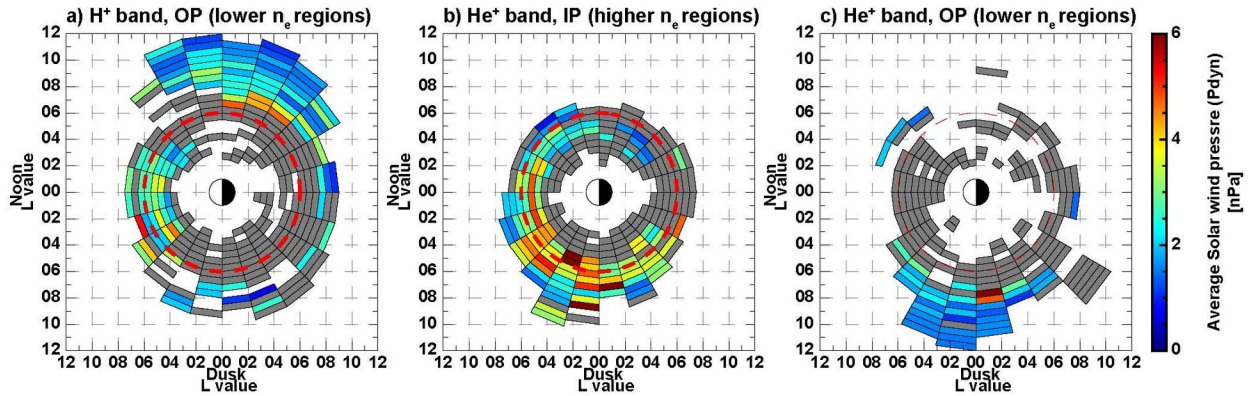


Figure 6. The spatial distribution of average solar wind dynamic pressure (P_{dyn}) corresponding to (a) H⁺ band, OP, (b) He⁺ band, IP, and (C) He⁺ band, OP.

3.3 Wave Properties of EMIC waves

In Section 3.1 and 3.2, we found significant dependence of EMIC wave occurrences on wavebands and relative locations from the plasmasphere, as well as geomagnetic conditions. In this section, we reveal their wave properties at different peak wave occurrence regions to

understand the characteristics of EMIC waves more further. To collect the pure wave properties for this analysis, we only consider our EMIC wave events which were satisfied with our criteria: wave power $> 10^{-3}$ nT²/Hz, polarization ratio, and coherence > 0.5 .

3.3.1 |MLAT| dependence of Polarization Sense ε and Wave Normal Angle θ

We computed the probability density function (PDF) for polarization sense ε and wave normal angle θ in separate bins of 2° absolute MLAT ($|\text{MLAT}|$) as shown in Figure 7. The PDF in the i th elementary interval of a given $|\text{MLAT}|$ bin is estimated as N_i/I , where N_i is the number of data points in this interval, and I is the total number of the data points in each $|\text{MLAT}|$ bins. The median values are calculated with a bin size of 2° in MLAT, marked as the black solid dashed lines.

In Figures 7a-7b, the median values of ε increase from -0.1 for H⁺ band outside the plasmasphere and -0.3 for He⁺ band inside the plasmasphere with increasing $|\text{MLAT}|$ until ε reaches 0 as linear polarity. This variation can be explained by EMIC wave mode conversion during propagation from the wave source to higher latitudes (Rauch and Roux, 1982; Young et al., 1981). Polarization reversal from LH to RH occurred at $|\text{MLAT}|=14^\circ$ for H⁺ band and $|\text{MLAT}|=22^\circ$ for the He⁺ band, respectively. These ε tendencies on $|\text{MLAT}|$ and polarization reversal $|\text{MLAT}|$ agree with previous observations that show the propagation effect of ε on $|\text{MLAT}|$ observed by the RBSP under different geomagnetic environments (e.g., Jun et al., 2019b; Yue et al., 2019). We also found that the median values of ε become almost linearly polarized ($|\varepsilon|<0.1$) after the polarization reversal $|\text{MLAT}|$ (Figures 7a-7c).

We consider the correction of the PDF of θ on $|\text{MLAT}|$ due to the decreasing solid angle for regularly distributed θ intervals in a narrow interval around lower $|\text{MLAT}|$. The appropriate analysis should be necessary using $\text{PDF}_\theta = \text{PDF} / \sin\theta$ (Santolik et al., 2016, Li et al., 2013, equation (1)). Figures 7d-7f shows the corrected PDF_θ of θ for H⁺ EMIC waves outside the plasmasphere, He⁺ EMIC waves inside the plasmasphere, and He⁺ EMIC waves outside the plasmasphere. The median values of θ show no significant variations with increasing $|\text{MLAT}|$. The PDF_θ of θ is mainly concentrated at $\theta=10$ - 30° with a $|\text{MLAT}|$ range of 0 - 45° , indicating that EMIC waves have the field-aligned direction from the magnetic equator to higher MLAT.

3.3.2 Spatial Distributions of EMIC Wave Properties

The spatial distributions of average EMIC wave power for each group are presented in Figure 8 in the same format as Figure 5. In general, He⁺ EMIC waves have stronger wave power than H⁺ EMIC waves, consistent with previous results (Saikin et al., 2016; Jun et al., 2019b). We found the most intense wave power of $10^{-1.5}$ nT²/Hz in the afternoon sector at $L=5$ - 7 for He band inside the plasmasphere (Figure 8b) compared to that at other peak occurrence regions. This region corresponds to the peak wave occurrences during the main phase with strong substorms and magnetospheric compressions, as shown in Figures 4f, 5b, and 6b. The waves associated with injected ions from the plasma sheet are enhanced during substorms/storms (Jun et al.,

2019a; Jordanova et al., 2001; Kozyra et al., 1984; Saikin et al., 2017; Tetrick et al., 2017). In Figure 8a, H⁺ EMIC waves outside the plasmasphere have stronger average wave power of 10^{-2.2} nT²/Hz at 10-14 MLT (noon sector) at L < 6 than those of 10^{-2.4} nT²/Hz at 4-8 MLT (morning sector) at L > 6. He⁺ EMIC waves outside the plasmasphere show an average wave power of 10^{-2.0} nT²/Hz at 15-21 MLT (dusk sector) at L > 8 in Figure 8c.

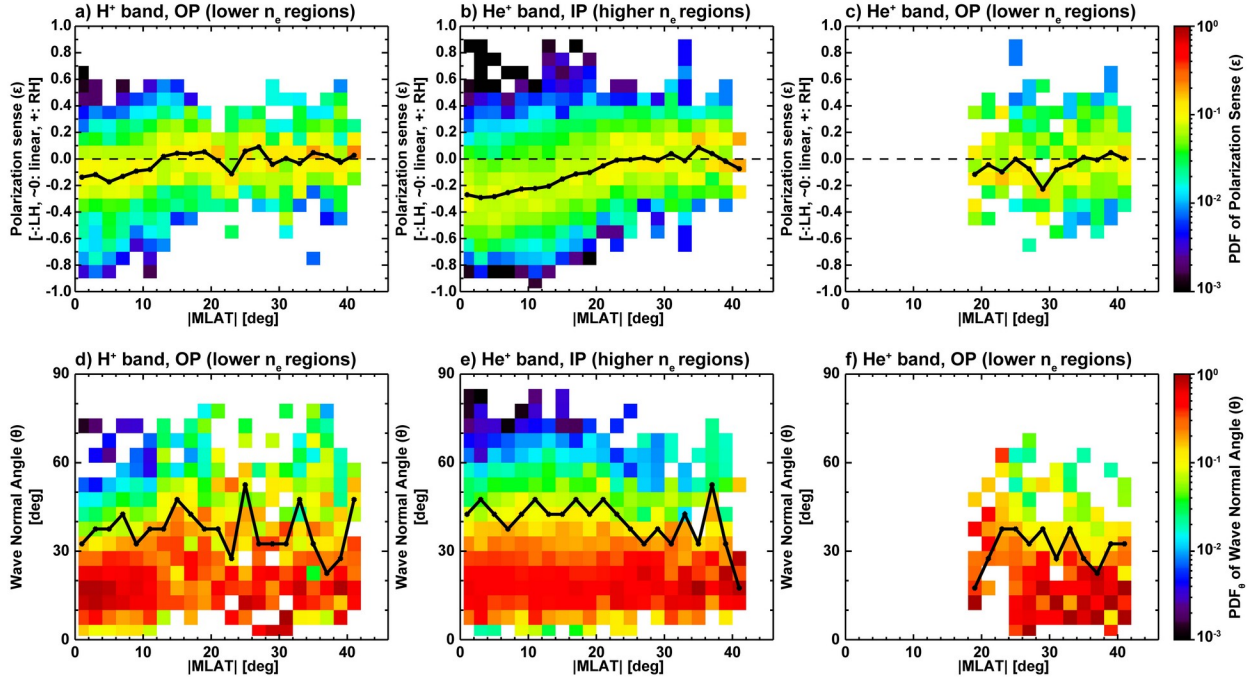


Figure 7. (a-c) Probability density function (PDF) of the polarization sense ε as a function of the $|MLAT|$ for H⁺ band, OP, He⁺ band, IP, and He⁺ band, OP; (d-f) corrected PDF_θ of wave normal angle θ for H⁺ band, OP, He⁺ band, IP, and He⁺ band, OP. The gray dots indicate the data points with a time resolution of 1 min. The black dots and solid line denote the median value with the MLAT bin size of 5°.

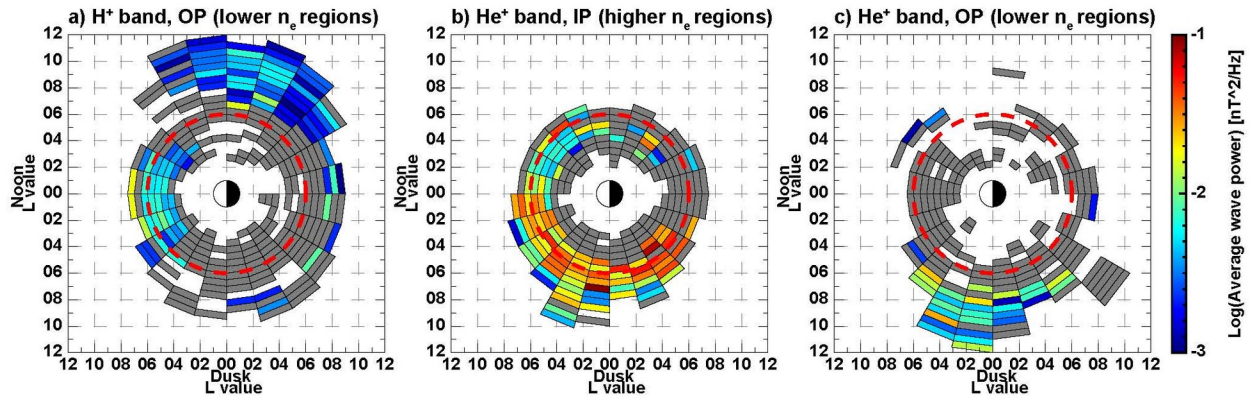


Figure 8. The spatial distribution of the wave power for (a) H⁺ band, OP, (b) He⁺ band, IP, and (c) He⁺ band, OP.

Figure 9 presents the spatial distribution of the polarization sense ε . We define LH EMIC waves as an average $\varepsilon < -0.1$ (bluish color), RH waves as an average $\varepsilon > 0.1$ (reddish color), and linear waves as an average $|\varepsilon| < 0.1$ (greenish color). For H^+ EMIC waves outside the plasmasphere (Figure 9a), ε varied between -0.1 and 0.2 at 4-8 MLT (morning sector) at $L > 8$, and between -0.3 and 0.1 at 10-14 MLT (noon sector) at $L < 7$ with their peak wave occurrence regions. A mixture of LH and linear in the noon sector is consistent with previous observations of linearly polarized in the H^+ band outside the plasmasphere (e.g., Jun et al., 2019b). For He^+ EMIC waves inside the plasmasphere (Figure 9b), an average value of ε is -0.3 (LH) at 10-14 MLT (noon sector) at $L < 6$ and -0.1 (LH) at 12-21 MLT (afternoon sector) at $L=5-8$. The LH EMIC waves in the noon sector agree with the previous observations showing a concentration of LH EMIC waves for He band near the wave source regions near the magnetic equator during the quiet conditions (e.g., Jun et al., 2019b). An average ε for He^+ EMIC waves outside the plasmasphere is approximately 0 (linear) at 15-18 MLT (dusk sector) at $L > 8$. These high ε values at higher L shells (4-8 MLT in Figure 9a, 12-21 MLT in Figure 9b, and 15-20 MLT in Figure 9c) are mainly observed at higher $|MLAT|$ as shown in Figure 2d, indicating that these observations may be due to mode conversion during propagation along the field line (Hu and Denton, 2009; Hu et al., 2010).

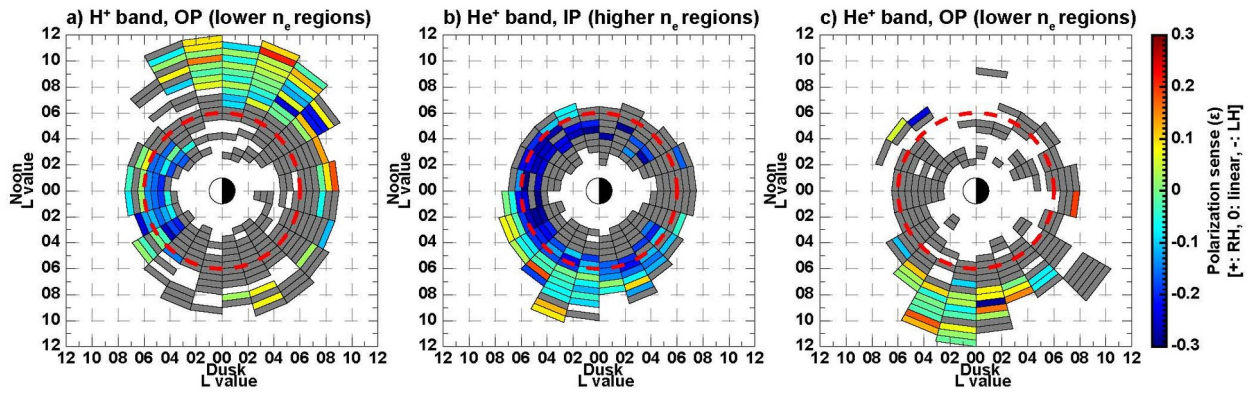


Figure 9. The spatial distribution of the polarization sense ε for (a) H^+ band, OP, (b) He^+ band, IP, and (c) He^+ band, OP.

The spatial distribution of wave normal angle θ is present in Figure 10. In general, we can see that most peak EMIC wave occurrence regions show the average θ of 28° , indicating the field-aligned directions as shown in Figures 7d-7f. In Figure 10a, the θ varied from 8° to 63° at 3-8 MLT at $L > 8$, indicating the mixture of field-aligned and oblique directions. For He^+ EMIC waves inside the plasmasphere, θ increases almost monotonically from 27° at 9 MLT to 32° at 21 MLT. There are two relatively lower θ regions at 10-14 MLT (noon sector) at $L < 6$ with an average value of 25° in Figure 10a, and at 16-19 MLT (dusk sector) at $L > 8$ with an average value of 23° in Figure 10c, respectively.

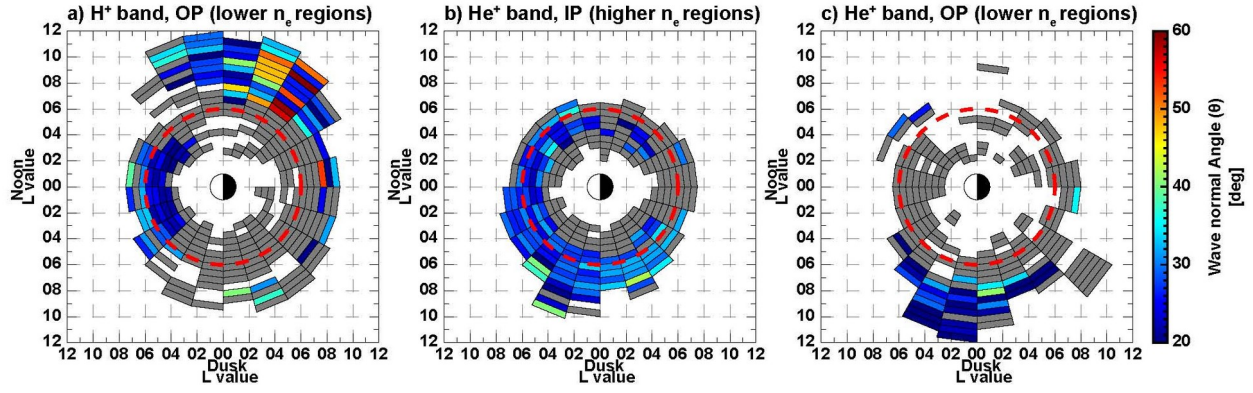


Figure 10. The spatial distribution of the wave normal angle θ for (a) H⁺ band, OP, (b) He⁺ band, IP, and (C) He⁺ band, OP.

4 Discussion

We have performed a comprehensive study of EMIC waves in the magnetosphere using RBSP and Arase observations from January 2017 to December 2018. We separated these EMIC waves into four groups (H^+ EMIC waves inside the plasmasphere, H^+ EMIC waves outside the plasmasphere, He^+ EMIC waves inside the plasmasphere, and He^+ EMIC waves outside the plasmasphere).

4.1 |MLAT| dependence of polarization sense ϵ

We found a significant relationship between the polarization sense ϵ which increases with increasing |MLAT|. This dependence of ϵ on |MLAT| is due to EMIC wave mode conversion during propagation along the field line from the magnetic equator to high magnetic latitudes. Initially, EMIC waves are generated with LH at the wave source regions. During propagation away from the equator, ϵ rapidly changes from LH to RH when the waves pass through the crossover frequency due to their dispersion relation (Rauch and Roux, 1982; Young et al., 1981). Previous observational studies suggested that the crossover location exists at |MLAT|= 10-17° (e.g., Loto'aniu et al. 2005; Jun et al. 2019b), which is similar to the current observations that polarization reversal occurred at |MLAT|=14° for H^+ band and |MLAT|=22° for the He^+ band.

We also found roughly constant polarization sense as linear after polarization reversal. In Figures 7d-7f, the PDF of wave normal angle is highly confined within $\theta=10-30^\circ$, indicating quasi-parallel direction. According to full-wave modeling done by Kim and Johnson (2016), polarization reversal appears near the crossover location from LH to linear. For quasi-parallel wave normal angle ($\theta < 30^\circ$), wave polarization keeps linear until the waves are totally reflected at the Buchsbaum resonance location toward higher L shell and lower magnetic latitude.

We are unable to clarify the different crossover |MLAT| between H^+ and He^+ bands in this study. One possible explanation is most likely due to the ion composition at which the wave event was observed. According to the cold dispersion relation of multi-ion ($H^+-He^+-O^+$) plasma, ion concentration play important role in deriving the crossover frequencies (Chen et al., 2013). In our observation, He^+ EMIC waves are the major EMIC wave activity inside the plasmasphere where cold plasma dominates. On the other hand, EMIC waves outside the plasmasphere are predominantly observed in the H^+ band, except for He^+ EMIC waves in the dusk sector outside the plasmasphere. Identifying the influence of ion concentration on the propagation effect to the EMIC wave properties is a compelling future research topic.

4.2 Possible generation processes of EMIC waves

In this study, we found four major wave occurrence regions: Region a (at the morning sector at $L > 8$ for H band); Region b (at the noon to postnoon sector at $L=3-7$ for H^+ and He^+ bands); Region c (at the afternoon sector at $L=5-7$ for He band); and Region d (at the dusk sector at $L > 8$ for He band). Table 1 summarizes the spatial distributions of EMIC waves with wave properties, and their dependence on geomagnetic activity. We discuss the characteristics and possible generation process of EMIC waves for each major wave occurrence region.

	Region a	Region b	Region c	Region d
Peak occurrence regions	03-08 MLT, $L > 8$, $ \text{MLAT} > 20^\circ$	10-14 MLT, $L = 4-7$, $ \text{MLAT} < 20^\circ$	12-18 MLT, $L = 6-8$, $ \text{MLAT} < 20^\circ$	16-18 MLT, $L > 8$, $ \text{MLAT} > 20^\circ$
Wave band, plasmopause location	H ⁺ , OP	1. H ⁺ , OP 2. He ⁺ , IP	He ⁺ , IP	He ⁺ , OP
Storm Phase	No storm	Recovery phase	Main phase	No storm
AL index (Substorm level)	~ -100 nT (Weak substorm)	~ -200 nT (Moderate substorm)	< -300 nT (Strong substorm)	~ -200 nT (Moderate substorm)
P_{dyn}	< 3 nPa	~ 3 nPa	> 3 nPa	< 2 nPa
Wave power [nT ² /Hz]	$10^{-2.4}$	1. $10^{-2.2}$ 2. $10^{-1.8}$	$10^{-1.5}$	$10^{-2.0}$
Polarization sense ϵ	-0.1 to 0.2 (Linear and RH)	1. -0.3 to 0.1 (Linear and LH) 2. ~ -0.3 (LH)	~ -0.1 (Linear)	~ 0 (Linear)
Wave normal angle θ	$\theta \sim 28^\circ$			

Table 1. Summary of spatial distributions of EMIC waves with wave properties, and their dependence on geomagnetic activity observed by the RBSP and Arase.

4.2.1 Region a: Morning sector at $L > 8$ in the H⁺ band

In our observation, the occurrence rate of EMIC waves in the H⁺ band is high at 4-8 MLT at $L > 8$ during the no storm interval associated with weak substorm periods (Figure 4b). Energetic plasma sheet protons (1-10 keV), considered to be the typical free energy source of

EMIC waves, are not sufficient to be the major contributor to the generation of EMIC waves in Region a under quiet conditions. One possible candidate of the free energy source is the temperature anisotropy by low-energy protons in the warm plasma cloak (< 1 keV), which was proposed by Keika et al. (2013) and Kim et al. (2016). Energetic protons with energies of > 10 keV drift from the premidnight to dusk (westward) due to the gradient and curvature drift motion. On the other hand, the protons in the energy range of < 10 keV, which consist of the warm plasma cloak (10-500 eV), are drifting toward the dawn side due to $E \times B$ drift, and they become the dominant population from premidnight to the dawn sector during active times. (e.g., Yue et al., 2016, 2017, and 2018). Even though our observation was mainly under quiet conditions, the warm plasma cloak protons can be one possible contributor to the generation of EMIC waves in the morning sector.

Recently, Teng et al. (2019) found unusual EMIC waves with a very narrow frequency bandwidth observed near the proton gyrofrequency. These waves are observed with enhanced suprathermal protons (10-100 eV) associated with magnetosonic waves. Magnetosonic waves can cause the resonant heating of suprathermal protons. The temperature anisotropy of suprathermal protons provides free energy for the generation of EMIC waves near the proton gyrofrequency in the low-density regions from dawn to dusk at the magnetic equator. In this region, the average bandwidth is 0.1 Hz, and the normalized frequency by the proton gyrofrequency varied from 0.23 to 0.95, indicating that some EMIC waves occurred with a narrow bandwidth near the proton gyrofrequency. Our observational result supports the result of Teng et al. (2019). We suggest that heating of suprathermal protons by the magnetosonic waves and the warm plasma cloak protons are a major driver of EMIC waves in the morning sector at higher L shells.

4.2.2 Region b: Noon sector at L=3-7 in the H⁺ and He⁺ bands

For H⁺ band, the wave occurrence rate outside the plasmasphere is high in the noon sector at L= 3-6 during the recovery phase of the storm (Figure 4h). These waves were associated with moderate substorm and solar wind dynamic pressure periods (Figures 5a and 6a). They have a mixture of LH and linear polarity with lower wave normal angle, consistent with linear H⁺ EMIC waves on the dayside, which are excited by enhancing solar wind dynamic pressure (e.g., Jun et al., 2019b). The solar wind dynamic pressure has been considered a major driver of EMIC waves on the dayside in hot plasma dominant region due to adiabatic heating by strong compression of the ambient magnetic field (e.g. Usanova et al., 2012; Keika et al., 2013; Park et al., 2016). The heating causes spreading of the energetic ions from the perpendicular to the parallel directions, appearing pancake-like in their velocity distribution, thus the increased temperature anisotropy provides a free energy source for H⁺ band EMIC wave excitation outside the plasmasphere (e.g., Olson and Lee, 1983; Anderson and Hamilton, 1993).

H⁺ EMIC waves in the noon sector is likely as a result of cyclotron resonance with the low-energy ions. According the the cold dispersion relation, we can assume the resonant energy E_R of the L-mode waves using the expression:

$$E_R \propto f_c / f_p (f / f_c)^2 / (1 - f / f_c)^3 \quad (1)$$

where f is the wave frequency, f_c is the gyrofrequency, and f_p is the plasma frequency (Kennel and Petschek, 1966). This means that energetic ions with the lower energy can be resonant with higher frequency waves. During the recovery phase, energetic ions at lower energy are refilling, while the flux of higher energetic ions decreases on the dayside the magnetosphere. Even though energetic protons at all energy ranges are increased temperature anisotropy due to adiabatic heating by solar wind dynamic pressure, the anisotropy at lower energy is higher than that at higher energy. In our observation, we found the center frequency varied from 0.7 Hz to 4.0 Hz for H^+ band outside the plasmasphere in the noon sector at $L=3-6$, which is the highest value of center frequency among all regions. Therefore, we suggest that the enhanced solar wind dynamic pressure causes adiabatic heating to lower-energy ions, leading to the generation of higher frequency H^+ EMIC waves outside the plasmasphere.

We found widely expanded regions of He^+ EMIC waves inside the plasmasphere at $L=5-7$ in the noon to postnoon sector during the recovery phase (Figure 4i). They have highly LH in the noon sector at $L<6$ within $|MLAT|<20^\circ$ and linear polarization in the postnoon at $L=6-8$ at $|MLAT|=20-40^\circ$, indicating that these waves are generated at the magnetic equator and they propagate to higher latitudes. Based on our observation, we suggest that He^+ EMIC waves are generated at broad and stable wave sources consisted of refilling cold plasmaspheric ions and coexisting hot ring current ions (e.g., Cornwall et al., 1970; Horne and Thorne, 1993; Kawamura et al., 1981; Jun et al., 2019a and 2019b). The plasmasphere can extend up to $L\sim 8$ under the extremely quiet conditions (Kwon et al., 2015), creating overlap regions with the ring current ions. In addition, the extended plasmaspheric plumes in the dusk sector during the recovery phase of the storm can provide cold plasmaspheric ions at higher L shells. These overlap regions can cause the strongest wave growth in the vicinity of density gradient during the recovery phase (e.g., Cornwall et al., 1970; Horne and Thorne, 1993).

4.2.3 Region c: Afternoon sector at $L=5-7$ in He^+ bands

We found that the majority of EMIC waves that occur during the main phase and associated with strong substorm periods are the He^+ band waves inside the plasmasphere. These waves exhibit the most intense wave power in the afternoon sector at $L=5-7$. During the main phase of the storm, magnetospheric convection causes the transport of the energetic plasma sheet particles into the inner magnetosphere. The strong temperature anisotropy is observed due to fresh particle injections over a broad range of energies > 1 keV in the cold plasma dominant regions. Based on the RBSP observation, Jun et al. (2019a and 2019b) found that He^+ EMIC waves inside the plasmasphere associated with injections are predominantly observed in the afternoon sector at $L=4.5-6.5$ with the most intense wave power. According to Equation (1), ions with higher energies are resonant with lower-frequency EMIC waves. Hot anisotropic ions control the growth rate of EMIC waves for the He^+ band, and cold plasma density leads to shifting the maximum growth rate of EMIC waves to lower frequencies (e.g., Chen et al., 2010; Cornwall et al., 1970; Kozyra et al., 1984; Lee et al., 2017).

4.2.4 Region d: Dusk sector at $L > 8$ in the He^+ bands

As mentioned previously, He^+ EMIC waves are commonly observed inside the plasmasphere, but we found that there is another peak wave occurrence region outside the plasmasphere in the dusk sector at $L > 8$ for He^+ band. Duskside He^+ band EMIC waves were also observed by THEMIS (Min et al., 2012). In this study, He^+ EMIC waves outside the plasmasphere have an average polarization sense ε and wave normal angle θ of ~ 0.0 (linear) and 23° at higher magnetic latitude ($|\text{MLAT}| > 20^\circ$), respectively. They were frequently observed under moderate geomagnetic conditions (i.e., no-storm interval or recovery phase of the storm, and the average AE and P_{dyn} of ~ -300 nT and ~ 3 nPa, respectively).

A possible process is off-equator EMIC waves (e.g., Allen et al., 2015, 2016; Vines et al., 2019). Vines et al. (2019) examined EMIC waves observed away from the magnetic equator at larger L shells ($L > 11$), using MMS observation. They showed bidirectional Poynting vectors in the location of the minimum in the magnetic field at higher magnetic latitudes, suggesting that MMS passed through off-equator EMIC wave source regions. During quiet conditions, off-equator and higher L shells can be possible generation regions for EMIC waves due to the combination of drift-shell splitting and Shabansky orbits caused by the compressed magnetic field on the dayside (McCollough et al., 2012). Energetic particles near the pitch angle of 90° can drift through the equator, while particles with smaller pitch angles are trapped between off-equatorial minima and the equator, executing Shabansky orbits on the dayside of the magnetosphere at outer L shells. The off-equatorial magnetic field minima becomes unstable for EMIC wave excitation due to increasing temperature anisotropy.

Based on our observations, we suggest that EMIC waves can be excited by different possible sources depending on their geomagnetic environments in the magnetosphere. Figure 11 presents a schematic picture of four major EMIC wave distributions with their characteristics and possible sources in the magnetosphere. In the morning sector at $L > 8$, EMIC waves are predominantly observed in the H band during the quiet geomagnetic conditions. We think that the free energy source of these waves would be the temperature anisotropy by suprathermal protons ($E < \text{several hundred eV}$). Suprathermal protons in the morning sector are supplied by eastward drifted warm plasma cloak or heating by magnetosonic waves. During the recovery phase of the storm, EMIC waves are mainly observed in the noon sector at $L = 3-7$ for both H and He bands. H EMIC waves outside the plasmasphere are generated due to adiabatic heating by magnetospheric compressions, while a mixture of cold plasmaspheric plasma and hot ring current ions are the free energy sources for He^+ EMIC waves in the noon to postnoon sector. The afternoon sector at $L = 5-7$ is the region of intense EMIC waves in the He^+ band during the disturbed geomagnetic conditions. The injected particles with temperature anisotropy act as the free energy sources for these waves. We suggest that duskside EMIC waves at $L > 8$ would be due to the temperature anisotropy by a combination of drift-shell splitting and Shabansky orbit at off-equator. For future work, it will be desirable to calculate the resonance conditions at the different regions and compare them to the in-situ plasma observations, in order to clarify EMIC waves generated through different processes work different roles for wave-particle interactions in the inner magnetosphere.

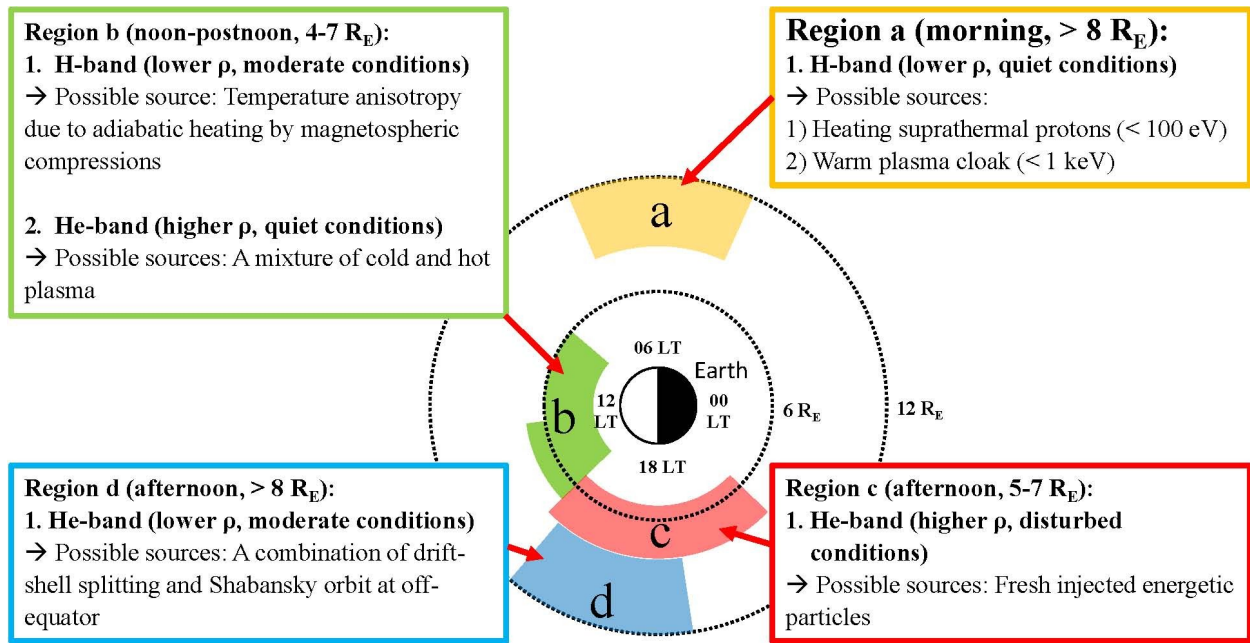


Figure 11. Schematic figure of the four major occurrence regions of EMIC waves in the magnetosphere.

5 Conclusions

In this study, we investigated the spatial distributions and wave properties of EMIC waves in the magnetosphere. We have identified EMIC wave events using the RBSP and Arase observations from January 2017 to December 2018. A total of 936.1 hrs of EMIC waves including 39 storm intervals was observed and we divided them into four groups by considering the waveband identified using the equatorial ion gyrofrequencies and satellite locations with respect to the plasmapause. The observational results are summarized as follows:

1. EMIC waves are mainly observed on the dayside magnetosphere and the wave occurrence at higher L shells ($L > 6$) is higher compared to that near the plasmasphere ($L < 6$).

2. H^+ EMIC waves outside the plasmasphere have two peak wave occurrence regions at 4-8 MLT at $L > 8$ in the morning sector and at 10-14 MLT at $L < 6$ in the noon sector. He^+ EMIC waves inside the plasmasphere show wider MLT coverage at 12-21 MLT and $L=6-8$. He^+ EMIC waves outside the plasmasphere are predominantly observed at 14-18 MLT and at $L > 8$ in the dusk sector.

3. During non-storm times, EMIC waves are frequently observed at higher L shells on the dayside, in particular having a concentration of H^+ EMIC wave outside the plasmasphere at 4-8 MLT and $L > 8$. He^+ EMIC waves inside the plasmasphere at 10-21 at $L=6-8$ are the predominant wave band during the main phase of the storm. He^+ EMIC waves have peak wave occurrences in the noon sector at $L < 7$ in the recovery phase of the storm.

4. H^+ EMIC waves outside the plasmasphere are frequently observed at 4-8 MLT at $L > 8$ during weak substorm and low solar wind dynamic pressure intervals. On the other hand, He^+ EMIC waves inside the plasmasphere at 12-21 MLT at $L=5-7$ prefer to be generated under disturbed conditions such as during strong substorms and magnetospheric compressions.

5. The median values of polarization sense ε is LH near the magnetic equator. ε approaches 0 (linear polarity) as $|MLAT|$ increases. Polarization reversal from LH to RH appeared at $|MLAT|=14^\circ$ for H^+ band and $|MLAT|=22^\circ$ for the He^+ band, respectively. The median values of ε become almost linearly polarized ($|\varepsilon| < 0.1$) after the polarization reversal $|MLAT|$. The wave normal angle θ has no significant dependence on $|MLAT|$ and is mainly concentrated at $\theta=10-30^\circ$.

6. He^+ EMIC waves inside the plasmasphere exhibit the most intense wave power at 12-21 MLT (afternoon sector) and at $L=5-7$, which is consistent with the peak wave occurrence regions during the main phase of the storm. In general, He^+ EMIC waves have more intense wave power than H EMIC waves.

7. EMIC waves for both H and He band at $L < 6$ exhibit LH and linear polarities in the range ε of -0.3 to 0.1 in the noon to afternoon sector. The ε at higher MLAT in the morning and dusk sector shows linear and RH polarities having relatively higher values of -0.1 to 0.2.

8. H^+ EMIC waves outside the plasmasphere at 3-8 MLT at $L > 8$ exhibits a variety of wave normal angle θ in the range of $8-63^\circ$. He^+ EMIC waves inside the plasmasphere show

monotonically increasing θ from 27° at 9 MLT and from 32° at 21 MLT. H^+ EMIC waves have relatively lower θ regions at 10-14 MLT (noon sector) at $L < 6$ and at 16-19 MLT (dusk sector) at $L > 8$.

In summary, our study has shown that EMIC waves have distinct characteristics at different wave occurrence regions in the magnetosphere. This result suggests that EMIC waves can be generated by different generation processes depending on their geomagnetic environments, which in turn affects a number of processes related to EMIC waves.

Acknowledgments

The Van Allen Probes data of the Level 3 EMFISIS magnetometer data was obtained from (<http://emfisis.physics.uiowa.edu/data/index>). Science data of the ERG (Arase) satellite was obtained from the ERG Science Center operated by ISAS/JAXA and ISEE/Nagoya University (<https://ergsc.isee.nagoya-u.ac.jp/index.shtml.en>, Miyoshi et al., 2018b). The present study analyzed MGF-L2 64 Hz v03.04, HFA-L2 v01.01, HFA-L3 v01_01 and Orbit L3 TS04 v01 data. The geomagnetic indices (AL, solar wind dynamic pressure, SYM-H) were obtained from the SPDF/Goddard Space Flight Center interface at <http://omniweb.gsfc.nasa.gov/>. Chao Yue gratefully acknowledges support from research grant National Key R&D Program of China 2020YFE0202100, NSFC Grant Numbers: 41974191 and China National Space Administration project D020303. This study is supported by JSPS KAKENHI (15H05815, 15H05747, 16H06286, 17H00728, 20H01959) and the JSPS-CAS bilateral project. Works of CJ, YM, SI, SN, MS are a part of ERG-Science.

References

- Allen, R. C. et al. (2015), A statistical study of EMIC waves observed by Cluster: 1. Wave properties. *Journal of Geophysical Research: Space Physics*, 120, 5574-5592. doi:10.1002/2015JA021333
- Allen, R. C. et al. (2016), A statistical study of EMIC waves observed by Cluster: 2. Associated plasma conditions. *Journal of Geophysical Research: Space Physics*, 121, 6458-6479. doi:10.1002/2016JA022541
- Anderson, B. J., Erlandson, R. E., & Zanetti, L. J. (1992a), A statistical study of Pc1-2 magnetic pulsations in the equatorial magnetosphere: 1. Equatorial occurrence distributions. *Journal of Geophysical Research*, 97(A3), 3075-3088, doi:10.1029/91JA02706
- Anderson, B. J., Erlandson, R. E., & Zanetti, L. J. (1992b), A statistical study of Pc1-2 magnetic pulsations in the equatorial magnetosphere: 2. Wave Properties. *Journal of Geophysical Research*, 97(A3), 3089-3101. doi:10.1029/91JA02706
- Anderson, B. J., & Hamilton, D. C. (1993), Electromagnetic ion cyclotron waves stimulated by modest magnetospheric compressions. *Journal of Geophysical Research*, 98, 11,369-11,382. doi:10.1029/93JA00605
- Arnoldy, R. L., et al. (2005), Pc1 waves and associated unstable distributions of magnetospheric protons observed during a solar wind pressure pulse. *Journal of Geophysical Research*, 101, A07229. doi:10.1029/2005JA011410
- Axford, W. I. (1969), Magnetospheric convection. *Reviews of Geophysics*, 7(1, 2), 421-459. doi:10.1029/RG007i001p00421
- Chen, L., Thorne, R. M., Jordanova, V. K., Wang, C.-P., Gkioulidou, M., Lyons, L., & Horne, R. B. (2010), Global simulation of EMIC wave excitation during the 21 April 2001 storm from coupled RCM-RAM-HOTRAY modeling. *Journal of Geophysical Research*, 115, A07209. doi:10.1029/2009JA015075.
- Cornwall, J. M., Coroniti, F. V., & Thorne, R. M. (1970), Turbulent loss of ring current protons. *Journal of Geophysical Research*, 75, 4699-4709. doi:10.1029/JA075i025p04699
- Engebretson, M. J., Peterson, W. K., Posch, J. L., Klatt, M. R., Anderson, et al. (2002), Observations of two types of Pc 1-2 pulsations in the outer dayside magnetosphere. *Journal of Geophysical Research*, 107(A12), 1451. doi:10.1029/2001JA000198
- Engebretson, M. J., Peterson, W. K., Posch, J. L., Klatt, M. R., Anderson, B. J., Russell, C. T., Singer, H. J., Arnoldy, R. L., & Fukunishi, H. (2012), Observations of two types of Pc 1-2 pulsations in the outer dayside magnetosphere. *Journal of Geophysical Research*, 107(A12), 1451. doi:10.1029/2001JA000198
- Halford, A. J., Fraser, B. J., & Morley, S. K. (2010), EMIC wave activity during geomagnetic storm and nonstorm periods: CRRES results. *Journal of Geophysical Research*, 115, A12248. doi:10.1029/2010JA015716
- Halford, A. J., Fraser, B. J., Morley, S. K., Elkington, S. R., & Chan, A. A. (2016), Dependence of EMIC wave parameters during quiet, geomagnetic storm, and geomagnetic storm phase times. *Journal of Geophysical Research: Space Physics*, 121, 6277-6291. doi:10.1002/2016JA022694
- Horne, R. B., & Thorne, R. M. (1993), On the preferred source location for the convective amplification of ion cyclotron waves. *Journal of Geophysical Research*, 98(A6), 9233-9247. doi:10.1029/92JA02972

- Horne, R. B., & Thorne, R. M. (1994), Convective instabilities of electromagnetic ion cyclotron waves in the outer magnetosphere. *Journal of Geophysical Research*, 99, 17,259-17,273. doi:10.1029/94JA01259
- Horne, R. B., and Miyoshi, Y. (2016), Propagation and linear mode conversion of magnetosonic and electromagnetic ion cyclotron waves in the radiation belts. *Geophysical Research Letters*, 43, 10,034–10,039, doi:10.1002/2016GL070216
- Hu, Y., & Denton, R. E. (2009), Two-dimensional hybrid code simulation of electromagnetic ion cyclotron waves in a dipole magnetic field. *Journal of Geophysical Research*, 114, A12217. doi:10.1029/2009JA014570
- Hu, Y., Denton, R. E., & Johnson, J. R. (2010), Two-dimensional hybrid code simulation of electromagnetic ion cyclotron waves of multi-ion plasmas in a dipole magnetic field. *Journal of Geophysical Research*, 115, A09218. doi:10.1029/2009JA015158
- Hyun, K., Kim, K.-H., Lee, E., Kwon, H.-J., Lee, D.-H., and Jin, H. (2014), Loss of geosynchronous relativistic electrons by EMIC wave scattering under quiet geomagnetic conditions. *Journal of Geophysical Research: Space Physics*, 119, 8357-8371. doi:10.1002/2014JA020234
- Jordanova, V. K., Farrugia, C. J., Thorne, R. M., Khazanov, G. V., Reeves, G. D., & Thomsen, M. F. (2001), Modeling ring current proton precipitation by electromagnetic ion cyclotron waves during the May 14-16, 1997, storm. *Journal of Geophysical Research*, 106, 7-22. doi:10.1029/2000JA002008
- Jordanova, V. K., Albert, J., and Miyoshi, Y. (2008), Relativistic electron precipitation by EMIC waves from self-consistent global simulations. *Journal of Geophysical Research*, 113, A00A10. doi:10.1029/2008JA013239
- Jun, C.-W., Yue, C., Bortnik, J., Lyons, L. R., Nishimura, Y., Kletzing, C., Wygant, J., & Spence, H. (2019a), A statistical study of EMIC waves associated with and without energetic particle injection from the magnetotail. *Journal of Geophysical Research: Space Physics*, 124, 1-18. doi:10.1029/2018JA025886
- Jun, C.-W., Yue, C., Bortnik, J., Lyons, L. R., Nishimura, Y. T., & Kletzing, C. A. (2019b), EMIC wave properties associated with and without injections in the inner magnetosphere. *Journal of Geophysical Research: Space Physics*, 124, 2029-2045. doi:10.1029/2018JA026279
- Kasaba, Y., Ishisaka, K., Kasahara, Y., Imachi, T., Yagitani, S., Kojima, H., et al. (2017), Wire probe antenna (WPT) and electric field detector (EFD) of Plasma Wave Experiment (PWE) aboard Arase: Specifications and initial evaluation results. *Earth, Planets and Space*, 69, 174. doi:10.1186/s40623-017-0760-x
- Kasahara, Y., Kasaba, Y., Kojima, H. et al. (2018), The Plasma Wave Experiment (PWE) on board the Arase (ERG) satellite. *Earth, Planets and Space*, 70, 86. doi:10.1186/s40623-018-0842-4
- Kawamura, M., Kuwashima, M., & Toya, T. (1981), Comparative study of magnetic Pc1 pulsations between low latitudes and high latitudes: Source region and propagation mechanism of the waves deduced from the characteristics of the pulsations at middle and low latitudes. *Memoirs of National Institute of Polar Research. Special issue*, 18, 83-100.
- Keika, K., Takahashi, K., Ukhorskiy, A. Y., & Miyoshi, Y. (2013), Global characteristics of electromagnetic ion cyclotron waves: Occurrence rate and its storm dependence. *Journal of Geophysical Research*, 118, 4,135-4,150. doi:10.1002/jgra.50385
- Kennel, C. F., and H. E. Petschek (1966), Limit on stably trapped particle fluxes. *Journal of Geophysical Research*, 71(1), 1-28.

- Kim, E.-H., & Johnson, J. R. (2016), Full-wave modeling of EMIC waves near the He⁺ gyrofrequency. *Geophysical Research Letters*, 43, 13-21. doi:10.1002/2015GL066978
- Kim, G.-J., Kim, K.-H., Lee, D.-H., Kwon, H.-J., and Park, J.-S. (2016), Occurrence of EMIC waves and plasmaspheric plasmas derived from THEMIS observations in the outer magnetosphere: Revisit. *Journal of Geophysical Research: Space Physics*, 121, 9,443-9,458. doi:10.1002/2016JA023108
- Kletzing, C. A., et al. (2013), The Electric and Magnetic Field Instrument Suite and Integrated Science (EMFISIS) on RBSP. *Space Science Reviews*, 179, 127-181. doi:10.1007/s11214-013-9993-6
- Kozyra, J.U., Cravens, T. E., Nagy, A. F., & Fonthelm, E. G. (1984), Effects of energetic heavy ions on electromagnetic ion cyclotron wave generation in the plasmopause region. *Journal of Geophysical Research*, 89, 2217-2233.
- Kumamoto, A., Tsuchiya, F., Kasahara, Y., Kasaba, Y., Kojima, H., Yagitani, S., et al. (2018), High frequency analyzer (HFA) of Plasma Wave Experiment (PWE) onboard the Arase spacecraft. *Earth, Planets and Space*, 70, 82. doi: 10.1186/s40623-018-0854-0
- Kuwashima, M., Toya, T., Kawamura, M., Hirasawa, T., Fukunishi, H., & Ayukawa, M. (1981), Comparative study of magnetic Pc1 pulsations between low latitudes and high latitudes: Statistical study. *Memoirs of National Institute of Polar Research. Special issue*, 18, 101-117.
- Kurth, W. S., De Pascuale S., Faden, J. B., Kletzing, C. A., Hospodarsky, G. B., Thaller, S. & Wygant, J. R. (2015), Electron densities inferred from plasma wave spectra obtained by the Waves instrument on Van Allen Probes. *Journal of Geophysical Research: Space Physics*, 120, 904-914. doi:10.1002/2014JA020857
- Kwon, H.-J., Kim, K.-H., Jee, G., Park, J.-S., Jin, H., & Nishimura, Y. (2015), Plasmopause location under quiet geomagnetic conditions (Kp<1): THEMIS observations. *Geophysical Research Letters*, 42, 7303-7310. doi:10.1002/2015GL066090
- Lee, D.-Y., Noh, S.-J., Choi, C.-R., Lee, J. J., & Hwang, J. A. (2017), Effect of hot anisotropic He⁺ ions on the growth and damping of electromagnetic ion cyclotron waves in the inner magnetosphere. *Journal of Geophysical Research*, 122, 4,935-4,942. doi:10.1002/2016JA023826
- Loto'aniu, T. M., Fraser, B. J., & Waters, C. L. (2005), Propagation of electromagnetic ion cyclotron wave energy in the magnetosphere. *Journal of Geophysical Research*, 110, A07214. doi:10.1029/2004JA010816
- Li, W., J. Bortnik, R. M. Thorne, C. M. Cully, L. Chen, V. Angelopoulos, Y. Nishimura, J. B. Tao, J. W. Bonnell, and O. LeContel (2013), Characteristics of the Poynting flux and wave normal vectors of whistler-mode waves observed on THEMIS. *Journal of Geophysical Research: Space Physics*, 118, 1,461-1,471. doi:10.1002/jgra.50176
- Matsuda, S., Kasahara, Y., Miyoshi, Y., Nomura, R., Shoji, M., Matsuoka, A., et al. (2018a), Spatial distribution of fine-structured and unstructured EMIC waves observed by the Arase satellite. *Geophysical Research Letters*, 45, 11,530-11,538. doi:10.1029/2018GL080109
- Matsuda, S., Kasahara, Y., Kojima, H., Kasaba, Y., Yagitani, S., Ozaki, M., et al. (2018), Onboard software of Plasma Wave Experiment aboard Arase: Instrument management and signal processing of waveform capture/onboard frequency analyzer. *Earth, Planets and Space*, 70, 75. doi:10.1186/s40623-018-0838-0
- Matsuoka, A., Teramoto, M., Nomura, R., Nosé, M., Fujimoto, A., Tanaka, Y., et al. (2018), The ARASE (ERG) magnetic field investigation. *Earth, Planets and Space*, 70, 43. doi:10.1186/s40623-018-0800-1

- Mauk, B. H., N. J. Fox, S. G. Kanekal, R. L. Kessel, D. G. Sibeck, and A. Ukhorskiy (2013), Science objectives and rationale for the radiation belt storm probes mission. *Space Science Reviews*, 179(1), 3-27. doi:10.1007/s11214-012-9908-y
- McCollough, J. P., Elkington, S. R., Usanova, M. E., Mann, I. R., Baker, D. N., & Kale, Z. C. (2010), Physical mechanisms of compressional EMIC wave growth. *Journal of Geophysical Research*, 115, A10214. doi:10.1029/2010JA015393
- McCollough, J. P., Elkington, S. R., & Baker, D. N. (2012), The role of Shabansky orbits in compression-related electromagnetic ion cyclotron wave growth. *Journal of Geophysical Research*, 117, A01208. doi:10.1029/2011JA016948
- Meredith, N. P., Horne, R. B., Kersten, T., Fraser, B. J., and Grew, R. S. (2014), Global morphology and spectral properties of EMIC waves derived from CRRES observations. *Journal of Geophysical Research: Space Physics*, 119, 5,328-5,342. doi:10.1002/2014JA020064
- Min, K., Lee, J., Keika, K., & Li, W. (2012), Global distribution of EMIC waves derived from THEMIS observations. *Journal of Geophysical Research*, 117, A05219. doi:10.1029/2012JA017515
- Miyoshi, Y., Sakaguchi, K., Shiokawa, K., Evans, D., Albert, J., Connors, M., & Jordanova, V. (2008), Precipitation of radiation belt electrons by EMIC waves, observed from ground and space. *Geophysical Research Letters*, 35, L23101. doi:10.1029/2008GL035727
- Miyoshi, Y., Shinohara, I., Takashima, T., Asamura, K., Higashio, N., Mitani, T., et al. (2018a), Geospace exploration project ERG. *Earth, Planets and Space*, 70, 101. doi:10.1186/s40623-018-0862-0
- Miyoshi, Y., Hori, T., Shoji, M. et al. (2018b) The ERG Science Center. *Earth, Planets, and Space* 70, 96. doi:10.1186/s40623-018-0867-8
- Miyoshi, Y., Matsuda, S., Kurita, S., Nomura, K., Keika, K., Shoji, M., et al. (2019). EMIC waves converted from equatorial noise due to $M/Q = 2$ ions in the plasmasphere: Observations from Van Allen Probes and Arase. *Geophysical Research Letters*, 46, 5662-5669. doi:10.1029/2019GL083024
- Moldwin, M. B., Downward, L., Rassoul, H. K., Amin, R., & Anderson, R. R. (2002), A new model of the location of the plasmopause: CRRES results. *Journal of Geophysical Research*, 107(A11), 1339. doi:10.1029/2001JA009211
- Morley, S. K., Ables, S. T., Sciffer, M. D., & Fraser, B. J. (2009), Multipoint observations of Pc1-2 waves in the afternoon sector. *Journal of Geophysical Research*, 114, A09205. doi:10.1029/2009JA014162
- Nakamura, S., Y. Omura, S. Machida, M. Shoji, M. Nosé, and V. Angelopoulos (2014), Electromagnetic ion cyclotron rising tone emissions observed by THEMIS probes outside the plasmopause. *Journal of Geophysical Research: Space Physics*, 119, 1,874-1,886. doi:10.1002/2013JA019146
- Olson, J. V., & Lee, L. C. (1983), Pc1 wave generation by sudden impulses. *Planetary and Space Science*, 31(3), 295-302. doi:10.1016/0032-0633(83)90079-X
- Park, J.-S., Kim, K.-H., Shiokawa, K., Lee, D.-H., Lee, E., Kwon, H.-J., Jin, H., & Jee, G. (2016), EMIC waves observed at geosynchronous orbit under quiet geomagnetic conditions ($Kp < 1$). *Journal of Geophysical Research*, 121, 1,377-1,390. doi:10.1002/2015JA021968
- Paulson, K. W., Smith, C. W., Lessard, M. R., Torbert, R. B., Kletzing, C. A., & Wygant, J. R. (2016), In situ statistical observations of Pc1 pearl pulsations and unstructured EMIC waves by the Van Allen Probes. *Journal of Geophysical Research: Space Physics*, 122, 105-119. doi:10.1002/2016JA023160

- Rauch, J. L., & Roux, A. (1982), Ray tracing of ULF waves in a multicomponent magnetospheric plasma: Consequences for the generation mechanism of ion cyclotron waves. *Journal of Geophysical Research*, 87(10), 8,191-8,198. doi:10.1029/JA087iA10p08191
- Remya, B., Lee, K. H., Lee, L. C., & Tsurutani, B. T. (2017), Coherency and ellipticity of electromagnetic ion cyclotron waves: Satellite observations and simulations. *Journal of Geophysical Research: Space Physics*, 122, 3,374-3,396. doi:10.1002/2016JA023588
- Saikin, A. A., Zhang J.-C., Allen, R. C., Smith, C. W., Kistler, L. M., Spence, H. E., et al. (2015), The occurrence and wave properties of H⁺-, He⁺-, and O⁺-band EMIC waves observed by the Van Allen Probes. *Journal of Geophysical Research: Space Physics*, 120, 7,477-7,492. doi:10.1002/2015JA021358
- Saikin, A. A., Zhang, J.-C., Smith, C. W., Spence, H. E., Torbert, R. B., & Kletzing, C. A. (2016), The dependence on geomagnetic conditions and solar wind dynamic pressure of the spatial distributions of EMIC waves observed by the Van Allen Probes. *Journal of Geophysical Research: Space Physics*, 121, 4,362-4,377. doi:10.1002/2016JA022523
- Saikin, A. A., Jordanova, V. K., Zhang, J. C., Smith, C. W., Spence, H. E., Larsen, B. A., et al. (2018), Comparing simulated and observed EMIC wave amplitudes using in situ Van Allen Probes' measurements. *Journal of Atmospheric and Solar-Terrestrial Physics*, 177, 190-201. <http://doi.org/10.1016/j.jastp.2018.01.024>
- Sakaguchi, K., Shiokawa, K., Ieda, A., Miyoshi, Y., Otsuka, Y., Ogawa, T., Connors, M., Donovan, E. F., & Rich, F. J. (2007), Simultaneous ground and satellite observations of an isolated proton arc at subauroral latitudes. *Journal of Geophysical Research*, 112, A04202. doi:10.1029/2006JA012135
- Sakaguchi, K., Shiokawa, K., Miyoshi, Y., Otsuka, Y., Ogawa, T., Asamura, K., & Connors, M. (2008), Simultaneous appearance of isolated auroral arcs and Pc 1 geomagnetic pulsations at subauroral latitudes. *Journal of Geophysical Research*, 113, A05201. doi:10.1029/2007JA012888
- Santolík, O., E. Macúšová, I. Kolmašová, N. Cornilleau-Wehrlin, and Y. de Conchy (2014), Propagation of lower-band whistler-mode waves in the outer Van Allen belt: Systematic analysis of 11 years of multi-component data from the Cluster spacecraft. *Geophysical Research Letters*, 41, 2,729-2,737. doi:10.1002/2014GL059815
- Shoji, M., Miyoshi, Y., Katoh, Y., Keika, K., Angelopoulos, et al. (2017), Ion hole formation and nonlinear generation of electromagnetic ion cyclotron waves: THEMIS observations. *Geophysical Research Letters*, 44, 8,730-8,738. doi:10.1002/2017GL074254
- Sibeck, D. G., McEntire, R. W., Lui, A. T. Y., Lopez, R. E., & Krimigis, S. M. (1987), Magnetic field drift shell splitting-Cause of unusual dayside particle pitch angle distributions during storms and substorms. *Journal of Geophysical Research*, 92, 13,485-13,497. doi:10.1029/JA092iA12p13485
- Takahashi, K., McEntire, R. W., Lui, A. T. Y., & Potemra, T. A. (1990), Ion flux oscillations associated with a radially polarized transverse Pc 5 magnetic pulsation. *Journal of Geophysical Research*, 95(A4), 3,717-3,731. doi:10.1029/JA095iA04p03717
- Teng, S., Li, W., Tao, X., Ma, Q., Wu, Y., Capannolo, L., et al. (2019), Generation and characteristics of unusual high frequency EMIC waves. *Geophysical Research Letters*, 46, 14,230-14,238. doi:10.1029/2019GL085220
- Tetrick, S. S., et al. (2017), Location of intense electromagnetic ion cyclotron (EMIC) wave events relative to the plasmopause: Van Allen Probes observations. *Journal of Geophysical Research*, 122, 4,064-4,088. doi:10.1002/2016JA023392

- Thorne, R. M. (2010), Radiation belt dynamics: The importance of wave–particle interactions. *Geophysical Research Letters*, 37, L22107. doi:10.1029/2010GL044990
- Tsurutani, B. T., et al. (2016), Heliospheric Plasma Sheet (HPS) impingement onto the magnetosphere as a cause of Relativistic Electron Dropouts (REDs) via coherent EMIC wave scattering with possible consequences for climate change mechanisms. *Journal of Geophysical Research: Space Physics*, 121, 10,130-10,156. doi:10.1002/2016JA022499
- Tsyganenko, N. A., and Sitnov, M. I. (2005), Modeling the dynamics of the inner magnetosphere during strong geomagnetic storms. *Journal of Geophysical Research*, 110, A03208. doi:10.1029/2004JA010798
- Usanova, M. E., Mann, I. R., Rae, I. J., Kale, Z. C., Angelopoulos, V., Bonnell, J. W., et al. (2008), Multipoint observations of magnetospheric compression–related EMIC Pc1 waves by THEMIS and CARISMA. *Geophysical Research Letters*, 35, L17S25. doi:10.1029/2008GL034458
- Usanova, M. E., et al. (2010), Conjugate ground and multisatellite observations of compression–related EMIC Pc1 waves and associated proton precipitation. *Journal of Geophysical Research*, 115, A07208. doi:10.1029/2009JA014935
- Usanova, M. E., Mann, I. R., Bortnik, J., Shao, L., and Angelopoulos, V. (2012), THEMIS observations of electromagnetic ion cyclotron wave occurrence: Dependence on AE, SYMH, and solar wind dynamic pressure. *Journal of Geophysical Research*, 117, A10218. doi:10.1029/2012JA018049
- Usanova, M. E., et al. (2014), Effect of EMIC waves on relativistic and ultrarelativistic electron populations: Groundbased and Van Allen Probes observations. *Geophysical Research Letters*, 41, 1,375-1,381. doi:10.1002/2013GL059024
- Usanova, M. E., Mann, I. R. and Darrouzet, F. (2016), EMIC Waves in the Inner Magnetosphere. *In Low-Frequency Waves in Space Plasmas (eds A. Keiling, D.-H. Lee and V. Nakariakov)*. doi:10.1002/9781119055006.ch5
- Vines, S. K., Allen, R. C., Anderson, B. J., Engebretson, M. J., Fuselier, S. A., Russell, C. T., et al. (2019), EMIC waves in the outer magnetosphere: Observations of an off–equator source region. *Geophysical Research Letters*, 46, 5,707-5,716. doi:10.1029/2019GL082152
- Wang, D., et al. (2015), Statistical characteristics of EMIC waves: Van Allen Probe observations. *Journal of Geophysical Research: Space Physics*, 120, 4,400-4,408. doi:10.1002/2015JA021089
- Wang, X. Y., et al. (2017), The occurrence and wave properties of EMIC waves observed by the Magnetospheric Multiscale (MMS) mission. *Journal of Geophysical Research: Space Physics*, 122, 8,228-8,240. doi:10.1002/2017JA024237
- Young, D. T., Perraut, S., Roux, A., de Villedary, C., Gendrin, R., & Jones, D. (1981), Wave-particle interactions near observed on GEOS 1 and 2 of ion cyclotron waves in He⁺-rich plasma Max-Planck-Institut für Katlenburg-Lindau 3, made with the ESA/GEOS 1 and 2 spacecraft which give an purpose. *Journal of Geophysical Research*, 86, 6,755-6,772. doi:10.1029/JA086iA08p06755
- Yue C., Zong, Q.-G., & Wang, Y. F. (2009), Response of the magnetic field and plasmas at the geosynchronous orbit to interplanetary shock. *Chinese Science Bulletin*, 54. doi:10.1007/s11434-009-0649-6
- Yue C., Zong, Q.-G., Zhang, H., Wang, Y. F., Yuan, C. J., Pu, Z. Y., et al. (2010), Geomagnetic activities triggered by interplanetary shocks. *Journal of Geophysical Research: Space Physics*, 115, A00I05. doi:10.1029/2010JA015356

- Yue C., Zong, Q., Wang, Y., Vogiatzis, I. I., Pu, Z., Fu, S., & Shi, Q. (2011), Inner magnetosphere plasma characteristics in response to interplanetary shock impacts. *Journal of Geophysical Research: Space Physics*, 116, A11206. doi:10.1029/2011JA016736
- Yue, C., Bortnik, J., Chen, L., Ma, Q., Thorne, R. M., Reeves, G. D., & Spence, H. E. (2017a), Transitional behavior of different energy protons based on Van Allen Probes observations. *Geophysical Research Letters*, 44(2), 625-633. doi:10.1002/2016GL071324
- Yue, C., Bortnik, J., Thorne, R. M., Ma, Q., An, X., Chappell, C. R., et al. (2017b), The characteristic pitch angle distributions of 1 eV to 600 keV protons near the equator based on Van Allen Probes observations. *Journal of Geophysical Research: Space Physics*, 122, 9,464-9,473. doi.org/10.1002/2017JA024421
- Yue, C., Bortnik, J., Li, W., Ma, Q., Gkioulidou, M., Reeves, G. D., et al. (2018), The composition of plasma inside geostationary orbit based on Van Allen Probes observations. *Journal of Geophysical Research: Space Physics*, 123, 6,478-6,493. doi:10.1029/2018JA025344
- Yue, C., Jun, C.-W., Bortnik, J., An, X., Ma, Q., Reeves, G. D., et al. (2019), The relationship between EMIC wave properties and proton distributions based on Van Allen probes observations. *Geophysical Research Letters*, 46, 4,070-4,078. doi:10.1029/2019GL082633